

**Mean streaming and the onset of turbulence in the reciprocating  
flow in a double bifurcation airway model: insights for  
high-frequency ventilation**

Chinthaka Jacob,\* David G. Tingay,<sup>†</sup> and Justin S. Leontini<sup>‡</sup>

## Abstract

High-frequency ventilation (HFV) is a medical ventilation technique which uses fast yet shallow inflations, resulting in small peak pressures, thereby protecting lungs from over-distension. While several mechanisms have been proposed for gas transport during HFV, this process is still not well understood and it is likely the treatment as it stands is sub-optimal. Nonlinear mean streaming and turbulent diffusion are two mechanisms with the potential to be further exploited for gas transport. Our previous study [Jacob *et al.* [1]] quantified these two mechanisms in a 1:2, or single-generation, bifurcating tube. That study showed that the generation of Dean vortices controlled the recirculating flux due to streaming and the onset of conditional turbulence. The primary aim of this study is to investigate these same mechanisms in a 1:2:4, or multi-generation, bifurcating tube, to systematically study and quantify the impact of coupling the flows between generations.

We show that the recirculating mass flux is less in the multi-generation case compared to the single-generation case due to the formation of Dean vortices during both the inhalation and exhalation flows. However, this recirculating flux still remains around 2% of the maximum flow rate. We show that this mean streaming mechanism is adequate to supply oxygen for a typical infant patient down to the 5th generation of the airway, however other mechanisms must be involved beyond this point.

Similar to the single-generation case, we show that turbulent bursts are possible in the first three generations of the airway and occur at times when the instantaneous flow rate exceeding a certain value. However, there is a clear dependence on both the upstream and downstream conditions that need to be accounted for in the generation, advection, and sustenance of turbulence. Further, the instability of Dean vortices at a peak flow rate is contrasted with the appearance of turbulence in a reciprocating flow in a straight pipe, which is driven by the Stokes boundary layers and occurs at peak deceleration.

The impact of the coupling between generations, and the importance of the consideration of the curvature of the geometry, both highlight the importance of considering an appropriate model geometry for physiological flows.

---

\* chinthaka.ravinatha@gmail.com; Faculty of Science, Engineering and Technology, Swinburne University of Technology, Melbourne, Victoria 3122, Australia

† david.tingay@rch.org.au; 1. Murdoch Children's Research Institute, 2. Neonatology, The Royal Children's Hospital, Melbourne, Victoria 3052, Australia

‡ jleontini@swin.edu.au; Faculty of Science, Engineering and Technology, Swinburne University of Technology, Melbourne, Victoria 3122, Australia

## A. Introduction

This paper reports on direct numerical simulations of the reciprocating flow through an in-plane double bifurcating tube. The primary objective of this study is to provide a generic model of the flows and subsequent gas transport in the human airway at conditions that are typically experienced during High-Frequency Ventilation (HFV) [2], a type of mechanical ventilation therapy routinely applied on patients with damaged or delicate lungs. HFV uses fast, low-tidal-volume inflations to achieve adequate gas exchange while simultaneously reducing peak intralung pressures to minimize over-distension and ventilator-induced injury. The low-volume inflations do not empty and refill the “dead space” of the airway and the success of HFV - or lack thereof - is therefore dependent on exploiting transport mechanisms other than bulk advection. Despite its extensive use and importance, the subtle gas exchange process involved is not completely understood [3].

In a previous direct numerical simulation study [1] of the reciprocating flow in a simpler single bifurcating tube, we have shown that two important potential transport mechanisms - nonlinear mean streaming, and the generation of conditional turbulence - are driven by the formation of Dean vortices (streamwise-oriented vortices generated via the centrifugal instability of the flow through the curved sections of the bifurcating tube) downstream of the bifurcation. Of course, in a single bifurcation these vortices only occur in any portion of the domain for half the reciprocating cycle as the downstream direction reverses. Here, we explicitly investigate the impact of coupling multiple generations together where these Dean vortices will occur in both directions in a given airway vessel - from the large vessels “above” during inhalation, and from the small vessels “below” during exhalation - on the mean streaming and generation of turbulence.

Beyond the primary application of this work to HFV and low-volume medical ventilation, the complex three-dimensional passage formed by a dichotomously branching network is a characteristic of mammalian anatomy. Fluid flows in such internal passages are pervasive in many biological systems, and the human cardiovascular and respiratory systems are important examples. Understanding flows in these systems is crucial as their malfunctioning is among primary causes of death worldwide [4, 5]. Besides, many existing engineering designs (e.g., pipe networks) and future engineered fractal-based micro-systems (e.g., bio-inspired heat exchangers based on the fish-gill morphology [6]) share the topology of successive bifur-

cations. Therefore, it is important to investigate the generic flow physics of dichotomously branching networks using an appropriate idealized configuration that is as simple as possible, but retains enough complexity to recreate the important flow features.

Earlier attempts of flow characterization in the human bronchial tree used simplified bifurcating branches [7, 8]. A large number of experimental and numerical studies have been carried out for this configuration using a steady inhalation flow [7]. Furthermore, the steady exhalation phase has attracted a similar interest due to its unique features such as the pressure drop and the role on the inhaled particle transport [9]. Attempts have been made to extrapolate these findings to predict the dynamics of oscillatory or reciprocating flow, treating it as a mere alternation between the inhalation and exhalation [10]. However, this may not be suitable due to significant unsteady effects present in the flow [11]. These unsteady effects are expected to increase at high breathing rates and therefore, flows at HFV conditions display unsteady flow dynamics [1].

The total area of the human airway increases at each subsequent bifurcation or airway generation, as the cross sectional area of each spawned vessel is more than half of that of the parent vessel. Therefore, the inertial forces (or equivalently the local Reynolds number) are highest in the early generations of the airway. Instantaneous and local Reynolds numbers in the trachea and upper generations of an infant airway undergoing HFV exceed those where turbulence is expected in a constant flow [12, 13]. Further, the dissimilar velocity fields formed between inhalation and exhalation, due to the curved flow path and varying cross sectional area in the bifurcating region result in a non-zero mean velocity at any given location in a purely reciprocating flow (even though the mean flux is by definition zero) which is known as nonlinear mean streaming or steady streaming [14, 15]. How these two phenomena - the generation of turbulence and nonlinear mean streaming - interact with the unsteady effects present in HFV is non-trivial, and describing this interaction is the primary objective of this paper.

It should also be mentioned that in addition to turbulent diffusion and nonlinear mean streaming, at least four other mechanisms are purported to play some role in the gas transport process of HFV - these are molecular diffusion, Pendulluft effect, cardiogenic mixing and Taylor dispersion [2, 16]. Here, we restrict our attention to turbulent diffusion and nonlinear mean streaming as they appear those most likely to provide significant transport over a range of scales.

Based on an order-of-magnitude analysis, Jan *et al.* [11] proposed a regime classification for respiratory patterns ranging from quiet breathing to HFV. This classification can be considered as a point of reference in predicting the characteristics of a given oscillatory flow based on two dimensionless parameters:  $L'/a$  and  $\alpha^2$ , where  $L'$  is the average axial displacement of a fluid particle,  $a$  is the airway radius and  $\alpha$  is the Womersley number ( $\alpha = a\sqrt{(\omega/\nu)}$ ). Three major zones, the unsteady (zone I), viscous (zone II) and convective (zone III), were identified in this space depending on the relative dominance of the convective acceleration terms or the viscous terms in the momentum transport equation. The convective zone is further divided into two subcategories (zone IIIa, zone IIIb) based on the experimental evidence. These two subdivisions correspond to the dominating convective acceleration term over the sub-dominant viscous term and the dominating convective acceleration term over the unsteady acceleration term respectively. Further, there is a turbulent region in the convective zone corresponding to high values of both  $L'/a$  and  $\alpha^2$ .

The panel (a) of Fig. 1 shows the parameter values used throughout this study, corresponding to conditions expected in the first 15 generations of the neonatal airway during HFV, superposed in the  $L'/a - \alpha^2$  parameter space where  $L'/a = Re_{max}/\alpha^2$ . The calculation of the parameter pairs for each generation is further explained in section B 4. According to this classification and the characteristics of the conditionally turbulent flow that we have previously reported in Jacob *et al.* [1], the airflow in the uppermost generation is most likely to experience turbulence due to high dimensionless amplitude and frequency of the flow. The conditional turbulence may lead to enhanced mixing and increased gas transport. The subsequent generations lie in the zone IIIa where convective acceleration terms dominate over the viscous term. At the lowest generation cases tested, modeling generations further down the airway, the flow becomes viscous dominated. Since the flows in the upper generations are in the convective region, and in this region the nonlinear convective terms are dominant, and these nonlinear terms can induce a mean flow correction, the mean streaming is expected to play a considerable role in the gas transport process [1] in these generations.

As further explained in section B 4, the simulation cases reported in this paper have been chosen to understand flow physics in different portions of the airway. This is achieved by varying the amplitude (Reynolds number) and the frequency (Womersley number) of the reciprocating flow via varying the inlet flow conditions. Due to the self-similar structure of the human airway and assuming symmetric flow splitting at each bifurcation, once the

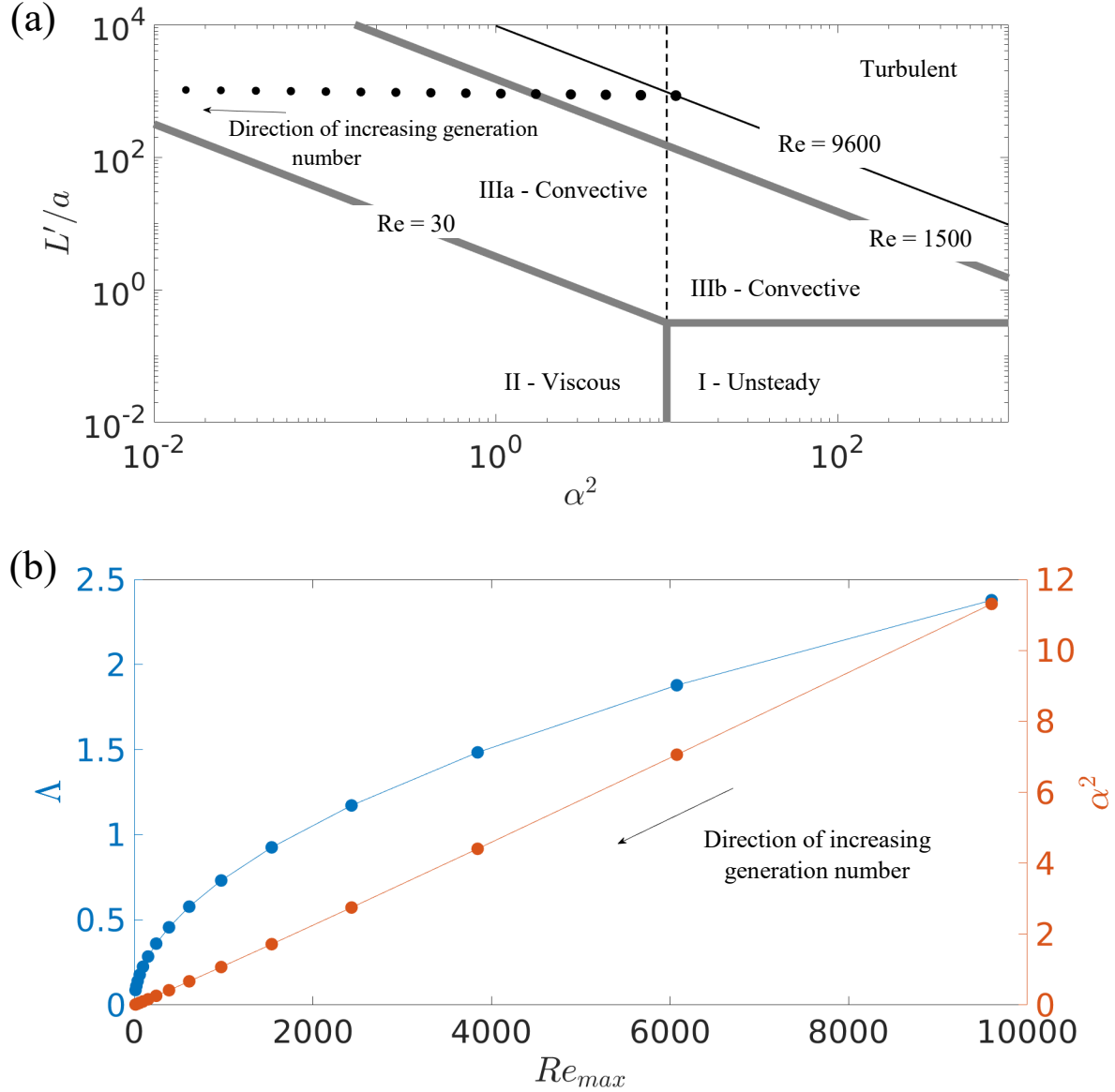


FIG. 1: Estimated conditions of the first 15 generations of the neonatal airway subjected to HFV ( $\bullet$ ), superposed on the flow regime diagram proposed by Jan *et al.* [11].

dimensionless amplitude and frequency (quantified by  $Re_{max}$  and  $\alpha^2$ ) are known at the first generation,  $Re_{max}$  and  $\alpha^2$  can be calculated at each subsequent generation. The panel (b) of Fig. 1 shows the  $Re_{max}, \alpha^2$  pairs representing each generation for the typical neonate conditions outlined in section B 4. Note that  $\Lambda$  is the Stokes parameter (defined in section B 2).

There are many oscillatory flow studies reported on model human bronchial tree networks of a wide range of complexities. Among these models, the patient-specific models developed from computed tomography (CT) imaging data [17] and computer generated asymmetric lung models [18] are the most complex and realistic ones. While, such realistic models apply to specific individuals, they are too complicated to be exploited in understanding of the generic flow physics. Therefore, generalized geometric models such as the Weibel model [19] and Horsfield model [20] are extensively used in studies where reporting generic fluid dynamic features is the priority. However, some recent studies have shown that these idealized geometries constructed based on Wiebel and Horsefield models have limitations and they cannot represent physiologically realistic airways. These limitations are discussed in section A 1.

The Weibel model of the human bronchial tree has been exploited by a majority of previously reported studies in this discipline [21]. Pertaining to various generations of this model, the branch diameter variation is such that the total cross-sectional area of a generation decreases from the zeroth generation ( $G_0$ ) to the third generation ( $G_3$ ) but increases thereafter, the cross-sectional area of  $G_4$  being equal to that of  $G_1$ . According to the Weibel model, the bronchial tree (originating from the trachea and ending in the alveolar sacs) comprises 23 generations of dichotomously branching airways. A single computation covering the entire bronchial tree is computationally resource intensive and many previous studies have therefore simulated only a part of it. For instance, Walters and Luke [22] developed a flow path ensemble method to determine the flow features in generations 4 – 12 of Weibel’s model. Similarly, Nowak *et al.* [23], used a 3.5 generation sub-unit model to study the fluid dynamics in up to 23 generations of a symmetric model. Kleinstreuer and Zhang [24] used adjustable triple bifurcation units to represent the particle deposition in a 16-generation model of the tracheobronchial tree.

### 1. *Limitations of this study and future work*

In light of limitations of using idealized airway geometries, the present study exploits another carefully chosen idealized airway configuration to investigate the evolution of the characteristic vortex structure emanating from each bifurcating junction and their interaction in a multi-generation setup.

## 2. Self-similar airway model used in the present study

In the present study, the 1:2:4 double-bifurcation geometry is considered as a minimal unit of the airway fractal structure that impacts the flow physics. The approximate self-similarity of the airway [8] is exploited in this study, meaning the geometric ratios between the first and second generations represented in the double bifurcation are similar. The motive of adopting a self-similar geometry here is that it enables us to probe the flow physics at any airway generation by using the same computational domain and simply changing the problem parameters as outlined in figure 1. The flow in a single 1:2 bifurcation in the context of a steady flow rate is reported by Pradhan and Guha [25]. In the context of a reciprocating flow pertinent to HFV, the flow in a single generation is reported in our previous study Jacob *et al.* [1] - the single generation was chosen for study first to deliberately remove the coupling between generations to focus on the flow features associated with flow through the curved bifurcating region. The present study extends these previous results by focusing on quantifying the effect of coupling between generations by exploiting the 1:2:4 bifurcation geometry. The direct comparison between a single- and double-generation model also allows an assessment of what “minimal unit” of the airway can be used that still captures the essential physics - we conjecture in this paper that all of the physical phenomena are present in the 1:2 bifurcation, but the double bifurcation is required to capture their important interaction, as the instability of the flow leading to turbulence is a strong function of both the upstream and downstream conditions.

Among a large number of oscillatory flow studies reported in the literature, we limit our focus to those studying flows with unsteady effects which are the most applicable to HFV. There are both experimental and numerical approaches pursued in this context. Menon *et al.* [26] exploited an experimental approach to measure velocity fields in a 1 : 3 model of the human airway. In this study, experiments at different peak Reynolds number  $Re_{max}$  and Womersley number  $\alpha$  were carried out and velocity profiles were measured at six different stations distributed through the model. The resulting flow distribution through the five secondary (lobar) bronchi was investigated for a range of oscillatory frequencies equivalent to 2.25 – 36 Hz in the actual airway. Similar results were reported in the early numerical study of Gatlin *et al.* [27]. Bauer *et al.* [3] performed a unique study supported by both experimental and computational approaches to investigate the flow phenomena associated

with conventional mechanical ventilation (CMV) and high-frequency ventilation (HFV), while appreciating similarities and differences of the basic flow features among CMV and HFV. Pertinent to their computational simulations of Lagrangian particle tracking, they reported an asymptotic saturation of the particle net displacement over cumulative flow cycles and established a linear relation between tidal volume and convective mass transport.

In a recently reported study, Jalal *et al.* [28] investigated the steady and oscillatory flow in a 3D printed realistic airway model using magnetic resonance velocimetry. The findings of this study were comprehensively analyzed, comparing with that of their previously reported studies performed on an idealized (in planar double bifurcation) model [29, 30]. In both steady and oscillatory flows, they reported increased dispersion and stronger secondary flows (the motion of fluid on a plane perpendicular to the streamwise direction) in the realistic airway model than that of the idealized one, while reporting a qualitatively similar mean flow topology in the steady flow. Interestingly, pertinent to HFV, the authors reported that steady streaming appeared not to be the primary gas transport mechanism.

Our previous study in the single bifurcation investigated the nonlinear mean streaming and onset of turbulence in the context of HFV Jacob *et al.* [1]. The amount of gas recirculated via mean streaming at various generations was reported, as well as the highest recirculating flux in the upper airway which is of the order of 5% of the peak flux. The gas transport among successive airway generations was ascribed to the mean recirculation regions formed by longitudinal vortices that are extended significantly downstream from the bifurcation (noting that the downstream direction reverses over the respiration cycle), caused by the centrifugal instability of the flow through the curved section of the bifurcation. Further, we reported conditional turbulence in the first three generations of the airway, that occurred in the flow leaving the bifurcation for a portion of the cycle centered around the peak flow rate. This phenomenon was conjectured to be due to an instability of the longitudinal vortices. This was contrasted to the appearance of turbulence in the reciprocating flow in a straight pipe which occurs not at peak flow rate but at peak deceleration via a bypass transition that is triggered by disturbances in the Stokes boundary layers [31–34].

The present study aims to investigate the role of these longitudinal vortices in generating nonlinear mean streaming and conditional turbulence in the context of coupling between generations - in a multi-generation model, the flows in intermediate airway vessels experience these vortices during both inhalation and exhalation. We match our simulation parameters

to those of our previous study in the single generation [1] with the aim of making a direct comparison of flow features while identifying coupling effects at various generation levels.

The paper is structured as follows. An overview of the simulation model and method is presented in section B. Section C presents the results first quantifying the mean streaming. We show that the mean streaming is reduced compared to the single generation, but is still significant in the first 5 generations, and that this streaming is caused by the generation of longitudinal vortices in the flow leaving the generation. Following this, results investigating the onset of turbulence are presented. These show the times and locations where turbulence occurs, indicating turbulence arises via an instability of the aforementioned longitudinal vortices. The mechanism for the generation of turbulence appears to be similar to that observed in the single generation model. However, the modification of the flow upstream and downstream due to the presence of other generations has a strong impact on the onset and sustained production of turbulence, showing multiple generations must be considered to fully understand the development of turbulence in this flow. Finally, the relevance of these results to the clinical application of HFV is discussed.

## B. Methodology

### 1. Flow domain and geometry configuration

The geometry employed throughout this study is a 1:2:4 symmetric planar bifurcating pipe. The human airway consists of 21 successively bifurcating generations [35, 36], and the geometry of these bifurcations is approximately geometrically similar, maintaining a constant ratio between the diameters of a predecessor pipe  $D_i$  and a successor pipe  $D_{i+1}$  of  $D_{i+1}/D_i = 0.79$ , and an included angle between the bifurcated successor pipes around  $\Theta = 64^\circ$  [8]. Figure 2 shows a schematic of the geometry employed. Pertinent to this geometry module, the branches from the top to bottom of the hierarchy are known as the mother branch, daughter branches and granddaughter branches in respiratory fluid mechanics.

Another aspect of the geometric similarity of the airway is the length of each branch section at the generation level  $i$  being approximately  $3.5D_i$  where  $D_i$  is the diameter of the corresponding branch section. While we have used this length for the intermediate (daughter) branches, we have used very long inlet and outlet sections in our computational

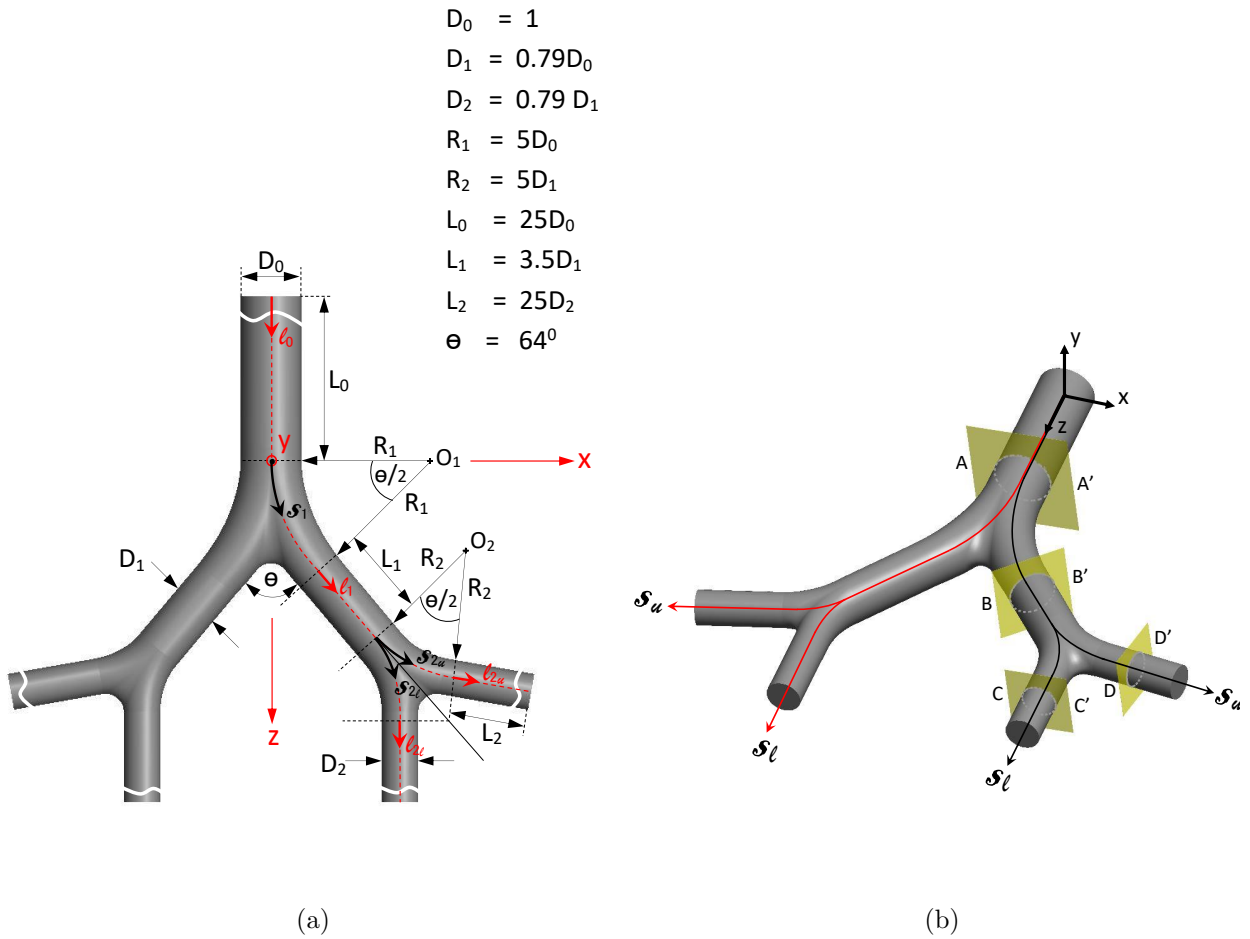


FIG. 2: Attributes of the bifurcation model used in the study. (a) Dimensions of the planar 1:2:4 bifurcation. (b) Three-dimensional CAD model of the 1:2:4 bifurcation. Note that the CAD model shown here is not to scale and the actual computational domain has much longer inlet and outlet sections to minimize the effect of boundary conditions on the flow generated by the bifurcation.

geometry to focus on the flow features generated by bifurcating junctions and intermediate generation without the influence of the boundary conditions.

The centerline of the mother branch coincides with the z-axis of the global coordinate system and splits into the two centerlines of the daughter branches. Each of these two centerlines of the daughter branches further splits into two, creating a total of four centerlines of the granddaughter branches. These centerlines coincide with branch axes in the cylindrical parts of the domain. Each axis of the successor branch is connected to its predecessor branch

by a smooth linearly varying arc (such that the radius of curvature of the outermost surface of the geometry is constant) to obtain the centerlines of the bifurcating region. These centerlines, denoted by  $S$ , with subscripts  $u$  and  $l$  indicating upper and lower branches, are used to identify streamwise locations of various cross sections. In this context, the axial velocity of any arbitrary point in the fluid domain is defined as the tangential component of the velocity vector to the closest centerline point. Therefore, the axial velocity  $\mathbf{U}_{ax}$  is identical to the streamwise velocity of the point of interest. The transverse velocity  $\mathbf{U}_{tr}$  is the projection of the velocity vector in a plane perpendicular to  $\mathbf{U}_{ax}$ .

## 2. Boundary conditions

Standard no-slip boundary conditions were applied at the rigid walls of the bifurcation, i.e.  $\mathbf{u} = 0$  and  $\partial p / \partial \mathbf{n} = 0$ , where  $\mathbf{u}$  is the flow velocity,  $p$  is the pressure and  $\mathbf{n}$  is the normal vector. Note that the use of rigid walls is somewhat justified physiologically, as the upper airway is cartilidge-reinforced and reasonably stiff [37].

The reciprocating flow with zero mean flux was driven by imposing a time-dependent boundary condition at the inlet (the free end of the mother branch) for the velocity, which was the analytical solution for the fully-developed laminar reciprocating flow in an infinitely long straight pipe first derived by Womersley [38]. A zero-normal-gradient condition ( $\partial p / \partial \mathbf{n} = 0$ ) was imposed for the pressure. This time-dependent velocity boundary condition distribution, assuming a harmonically-oscillating pressure gradient  $-\rho^{-1} \partial p / \partial z = K e^{i\omega t}$  is given by,

$$u(r, t) = R[U(\eta, \Lambda) e^{i\gamma}] = R[|U(\eta, \Lambda)| e^{i(\gamma+\theta)}], \quad (1)$$

where

$$U(\eta, \Lambda) = -iK\omega^{-1}[1 - J_0(\beta\Lambda\eta)/J_0(\beta\Lambda)], \quad (2)$$

and  $J_0$  is the Bessel function of the first kind, order 0 and

$$\gamma = \omega t, \eta = 2r/D, \beta = 2^{\frac{1}{2}} e^{\frac{3}{4}\pi i}. \quad (3)$$

The amplitude of the spatial mean velocity across the cross-section is given by

$$\hat{U} = K\omega^{-1}|1 - (2/\beta\Lambda)J_1(\beta\Lambda)/J_0(\beta\Lambda)|. \quad (4)$$

In these expressions,  $D$  is the branch diameter,  $r$  the radial coordinate,  $\Lambda$  the Stokes parameter defined in equation 7 and  $\theta$  the phase lag.

At the free end of the granddaughter branches, a modified outflow condition was imposed. Here a Dirichlet condition was imposed on the pressure ( $p = 0$ ), while nominally a zero-normal-gradient condition was imposed on the velocity ( $\partial\mathbf{u}/\partial\mathbf{n} = 0$ ). However, an extra divergence term was added to the velocity to prevent flow entering the domain through this boundary which numerically stabilizes the solution. Locally this means the mass conservation was not satisfied; however the impact of this was evident only within  $3 - 4$  diameters of the boundary, and the use of long granddaughter sections means this did not pollute the simulation results near the bifurcation. We have previously used this boundary condition successfully in studies of a 1:2 bifurcation [1], and it has previously been used successfully in other biologically-inspired oscillating flows in the same code [39].

### *3. Discretization and solver details*

The three-dimensional incompressible Navier-Stokes equations were solved in the flow domain described in section B 1 with the boundary conditions described in section B 2 using the spectral-element code Nek5000 [40]. The code has previously been employed and validated for use in oscillatory confined flows [41, 42]. Further details of the implementation details can be found in Tufo and Fischer [43], while an overview of the essential elements of the numerical scheme is provided below.

Like all finite-element based schemes, the code solves the equations of motion in a weak form. To facilitate this, we employed 7<sup>th</sup>-order tensor-product Lagrange polynomials for DNS1 - DNS4 and 5<sup>th</sup>-order tensor-product Lagrange polynomials for DNS5 (as outlined in the table I) associated with Gauss-Legendre-Lobatto quadrature points as both test and trial functions on a mesh of hexahedral elements that were free to have curved faces to exactly represent the curved surfaces of the bifurcation geometry.

Temporal discretization was done by first employing three-way time-splitting to arrive at separate sub-step equations for the advection, pressure and viscous terms of the Navier-Stokes equations. The advection equation was discretized and integrated using a third-order Adams-Bashforth scheme to arrive at an intermediate velocity field. Continuity was then imposed at the end of the pressure sub-step to arrive at a Poisson equation for the pressure

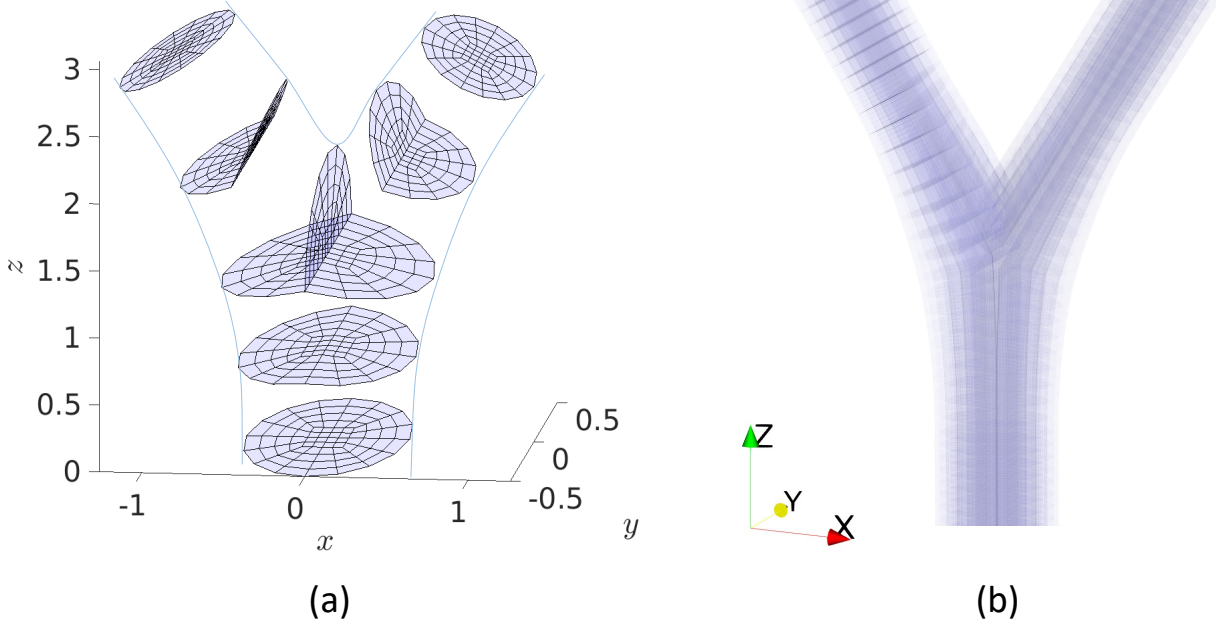


FIG. 3: The mesh topology of a bifurcating junction used in the study. (a) Macro mesh topology of a bifurcating junction. (b) Resulting mesh topology of hexahedral elements associated with Gauss-Legendre-Lobatto quadrature points of 7<sup>th</sup>-order tensor-product Lagrange polynomials.

correction, which once solved, provided a pressure field so the pressure sub-step equation could be integrated to a second intermediate velocity field. Finally, the diffusion term was integrated using a second-order Crank-Nicolson scheme to arrive at the velocity field at the end of the time step.

A resolution study was carried out to determine the required spatial and temporal resolution to resolve the flow. The same spatial and temporal resolution is used for all the simulations. Concerning the spatial resolution of the macro mesh, each branch contained 160 hexahedral elements in the transverse plane and in the streamwise direction, the spatial resolution is set in a way that the corresponding Kolmogorov length scale at each generation level is greater than the smallest mesh spacing. The structure of the macro element mesh on the transverse planes in a bifurcating region is shown in figure 3.

This resolution results in a mesh of 49,920 elements with a total of 17,122,560 node points. This setup was typically solved using 768 CPUs, with run times of around three weeks to conduct enough cycles of the flow to ensure converged statistics.

TABLE I: Summary of simulation attributes

Case	Simulating junction	${}^iG_{i+1}$	$L_0/D_0$	$L'/a$	$Re$	$\alpha^2$	$\Lambda$
DNS1		${}^0G_2$		25	849	9600	11.31
DNS2		${}^1G_3$		25	861	6076	7.06
DNS3		${}^2G_4$		25	873	3846	4.41
DNS4		${}^3G_5$		25	885	2434	2.75
DNS5		${}^8G_{10}$		25	950	247	0.26
							0.36

#### 4. Simulation parameters

Since the geometry used is fixed, and the reciprocating flow employed is purely harmonic, the flow can be shown to be a function of only two non-dimensional groups. The first of these essentially quantifies the amplitude of the reciprocating flow, which we define as a maximum Reynolds number

$$Re_{max} = \hat{U}_{max} D_0 / \nu \quad (5)$$

where  $\nu$  is the kinematic viscosity. The second parameter quantifies the frequency, which can be presented in terms of the square of the Womersley number

$$\alpha^2 = \frac{2\pi f D_0^2}{4\nu} \quad (6)$$

where  $f$  is the frequency of oscillation, or a traditional Stokes parameter

$$\Lambda = \frac{D}{2\delta} \quad (7)$$

where  $\delta = \sqrt{2\nu/(2\pi f)}$  is the Stokes layer thickness.

To set these parameters to be clinically relevant we start from the conditions of a typical full-term neonate, which are: volume per inflation per unit body weight of the infant 1 – 3 ml/kg and the frequency of therapy in the range of 5 – 15 Hz [44]. The typical diameter of the endotracheal tube employed is 3 mm. Assuming typical numbers of a body mass of 3kg and a ventilator frequency of 12Hz results in  $Re_{max} = 9600$  and  $\alpha^2 = 11.31$  at the mother branch of the first generation, referred to here as  ${}^0G_2$ .

The maximum local Reynolds number decreases from the predecessor generation  $Re_i$  to the successive generation  $Re_{i+1}$  by a factor of  $D_i/(2D_{i+1}) \approx 0.63$  while the Womersley

number decreases from the predecessor generation  $\alpha_i$  to the successive generation  $\alpha_{i+1}$  by a factor of  $D_{i+1}/D_i = 0.79$ . This reduction of  $Re_i$  and  $\alpha_i$  with increasing generation number  $i$  is caused by the reduction of local diameter in a given airway branch but an increase in the total area of each successive generation leading to a reduction of the local maximum velocity.

We therefore characterize the airflow at a particular airway generation subjected to HFV as a two-parameter problem in the  $Re_{max} - \alpha^2$  space. In this two-parameter space, we have taken the pairs identified in the panel (b) of figure 1 to match the conditions at each airway generation and run simulations matching the conditions of the first 9 generations.

### C. Results and Discussion

In this section we present the results of the simulations of the  $Re_{max}, \alpha^2$  parameter pairs shown in figure 1 and table I. Throughout, we use the term inhalation to refer to the flow moving from upper generations to lower generations (i.e. from the mother branch to daughter and granddaughter branches), and exhalation to refer to the flow moving in the opposite direction. Note that these terms here simply indicate flow direction - they do not imply any active or passive changes in pressure as may be the case in a physiological setting. We first present results quantifying the nonlinear mean streaming induced by the reciprocating flow, before investigating the appearance and character of turbulence.

#### 1. Streaming velocity

In this section, we focus on the quantification of mean streaming when a branch of a particular airway generation is coupled with neighbouring branches of upstream and downstream generations. We compare the resulting strength of the streaming with our previously reported study of a single 1:2 bifurcation which by definition does not have coupling effects [1] and hence quantify the effect of coupling between generation levels.

The streaming velocity field is simply the cycle-average of the velocity field,  $\bar{\mathbf{u}}$  which is directly calculated by averaging over the second cycle of the flow simulation. We excluded the first cycle of the simulation to avoid any initial transient. We also note that any transient did not appear to extend beyond this first cycle, with the statistics of the flow apparently

settled from the second cycle onward. In this context, the time scale of the oscillation of the flow cycle is much longer than the advective time scale  $L_{dom}/U$  where  $L_{dom}$  is the length of the computational domain. Therefore, we conclude that any transient appears in the flow has many advective time units to wash out of the domain even in a single cycle of oscillation.

The streaming velocity field for cases  ${}^0G_2$ ,  ${}^1G_3$ ,  ${}^2G_4$  and  ${}^8G_{10}$  are shown in Fig.4. This figure presents contours of the streaming velocity component aligned with the local axial direction (the tangential component of the velocity vector to the closest centerline point)  $\bar{U}_{ax}$  with positive  $\bar{U}_{ax}$  designating inhalation. In each of the four cases, the first panel displays 9 sections perpendicular to the streamwise direction accompanied by a plane passing through centerlines of all the branches. The second panel shows the same data without the latter center plane to clearly show the structure on the perpendicular planes. Note that the integral of  $\bar{U}_{ax}$  over an arbitrary cross section is zero as the  $\bar{U}_{ax}$  field is computed from the cycle-average of the zero-net-mass-flux reciprocating flow.

Figure 5(a-c) shows the mean flow axial vorticity  $\bar{\omega}_{ax}$ . Its structure is qualitatively similar between the  ${}^0G_2$ ,  ${}^1G_3$  and  ${}^2G_4$  cases. A general characteristic of these three cases is that along the core of the mother branch there are 8 counter-rotating vortices near the bifurcating junction, decaying to 4 counter-rotating vortices away from the bifurcation. These 8 counter-rotating vortices appear as a consequence of merging 4 counter-rotating vortices from each of the two daughter branches in the exhalation flow [Fig.18]. Along the core of the daughter branches, there are 4 counter-rotating vortices. Along the core of the granddaughter branches, there are 4 counter-rotating vortices near the bifurcating junction and their strength decreases with the distance measured from the bifurcating junction.

The vortex structure composed of 4 counter-rotating vortices observed in the mother branch of Fig.5(a-c) is qualitatively similar to that reported by Jacob *et al.* [1] for the single bifurcation. Further, the vortex structure composed of 2 counter-rotating vortices observed in the granddaughter branches of Fig.5(a-c) is qualitatively similar to the vortex structure of daughter branches reported by Jacob *et al.* [1]. This means that the vortex structure at each end is qualitatively similar between 1:2 and 1:2:4 bifurcation models. This similarity suggests that intergenerational coupling is likely to be weak beyond one generation and the double bifurcation likely captures the essential qualities of the flow in the airway.

These vortical structures are generated by a centrifugal instability of the flow when the fluid is subjected to centrifugal forces due to the curvature of the flow path. When the fluid

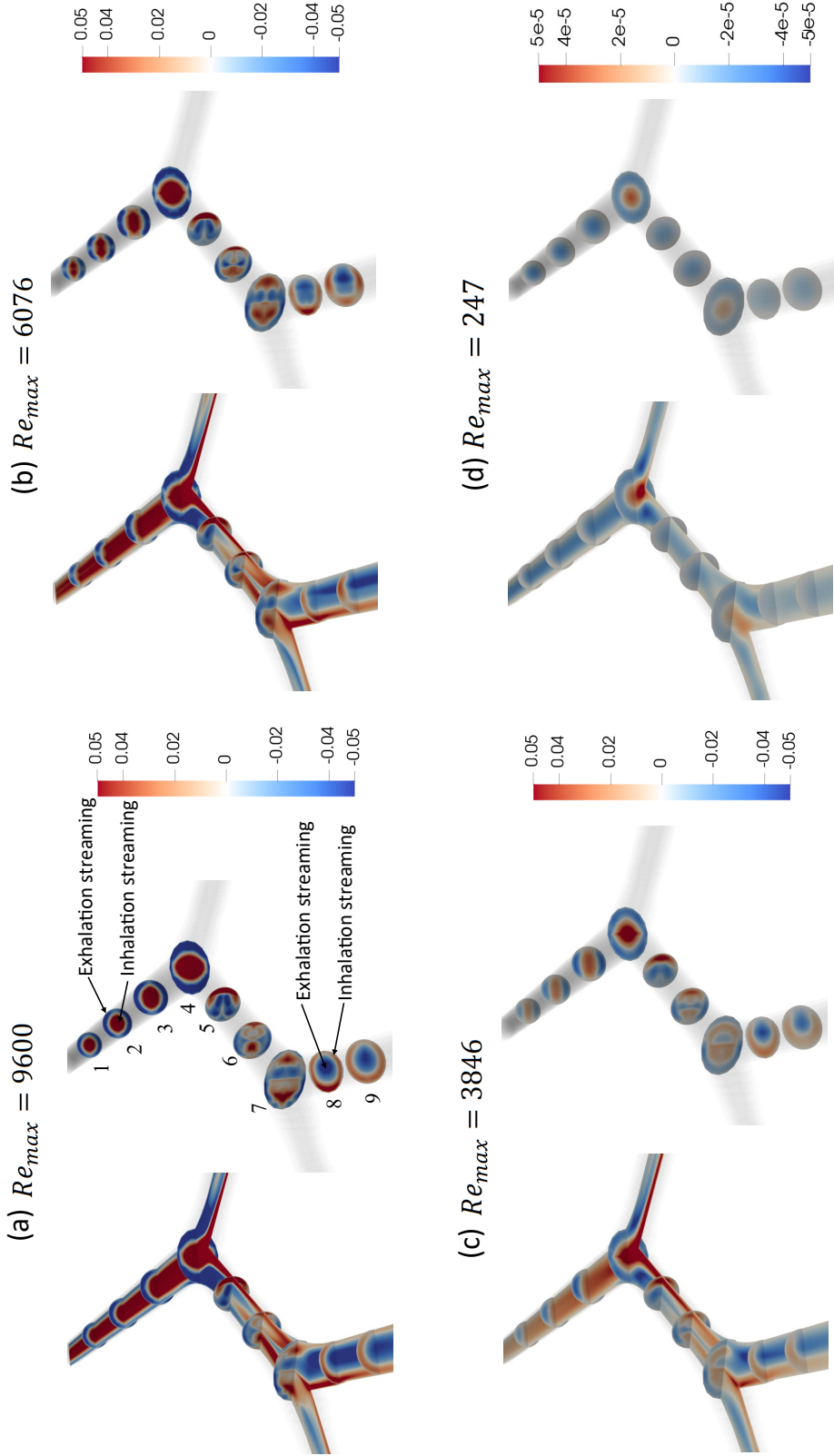


FIG. 4: Visualization of dimensionless streaming velocity  $\bar{\mathbf{U}}_{ax}/\hat{U}_{max}$  fields for (a)  ${}^0G_2$ , ( $Re_{max} = 9600, \alpha = 3.36, L/a = 849$ ); (b)  ${}^1G_3$ , ( $Re_{max} = 6076, \alpha = 2.66, L/a = 861$ ); (c)  ${}^2G_4$ , ( $Re_{max} = 3846, \alpha = 2.1, L/a = 873$ ); and (d)  ${}^8G_{10}$ , ( $Re_{max} = 247, \alpha = 0.51, L/a = 950$ ). The first panel of each case shows the longitudinal symmetry plane along with several transverse planes. The second panel shows the same field without the longitudinal symmetry plane.

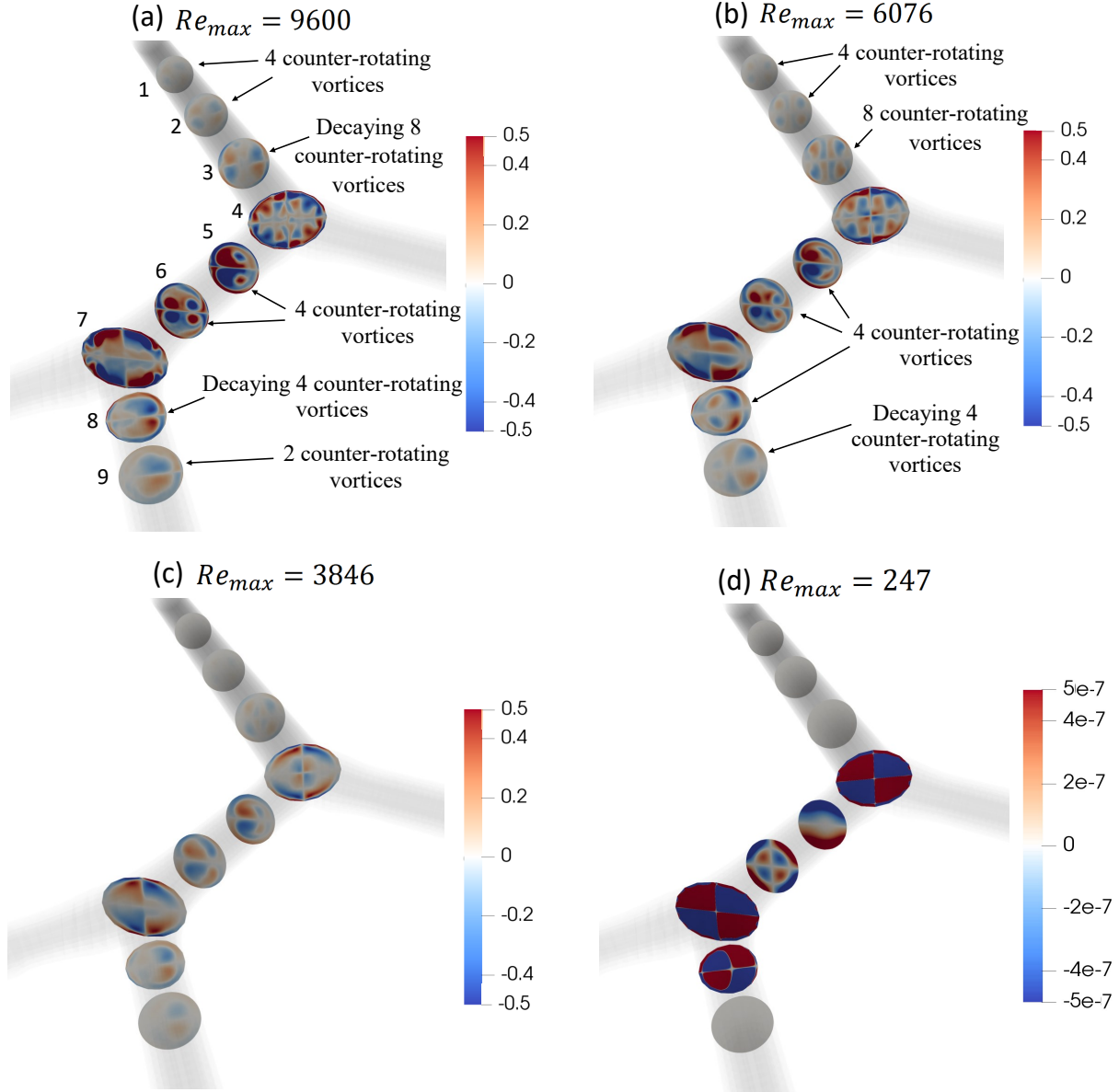


FIG. 5: Visualization of dimensionless axial vorticity  $\bar{\omega}_{ax}/\bar{\omega}_{max}$  (where  $\bar{\omega}_{max} = \hat{U}_{max}/D_0$ ) computed based on the streaming velocity  $\bar{U}_{ax}$  fields for (a)  ${}^0G_2$ , ( $Re_{max} = 9600$ ,  $\alpha = 3.36$ ,  $L/a = 849$ ); (b)  ${}^1G_3$ , ( $Re_{max} = 6076$ ,  $\alpha = 2.66$ ,  $L/a = 861$ ); (c)  ${}^2G_4$ , ( $Re_{max} = 3846$ ,  $\alpha = 2.1$ ,  $L/a = 873$ ); and (d)  ${}^8G_{10}$ , ( $Re_{max} = 247$ ,  $\alpha = 0.51$ ,  $L/a = 950$ ).

is flowing in a circular pipe of constant curvature, the centrifugal force pushes the fluid from the inner to the outer side of the curve in the plane of the curvature, and fluid returns along the upper and lower surfaces of the circular pipe generating two symmetric counter-rotating vortices. This mechanism was originally proposed by Dean [45] and has been reported to be

relevant in the bifurcation geometry as well [1, 11, 30].

Along the core of the mother branch, there is a strong inhalation streaming flow surrounded by an exhalation streaming. When the Reynolds number decreases (from panel a to c of Fig.4), the strength of the inhalation streaming gradually decreases in this region and spreads out along the plane passing through the centrelines of all branches. As shown by Fig.5(a-c), this region comprises of 8 counter rotating vortices near the bifurcation and rearranges to 4 clearly visible counter rotating vortices a short distance away from the bifurcation.

Along the inner core of the intermediate (daughter) branches of the first three cases (Fig.4(a-c)), there is a vertical semi-annular region of inhalation streaming located along the wall at the outside of the turn which is weakening in the direction of section 5 to 6. Simultaneously, there is another circular region of inhalation streaming closer to the wall at the inside of the turn which is strengthening in the same direction. Concurrently, there is a region of exhalation streaming that surrounds these two regions of inhalation streaming. This exhalation streaming region eventually diffuses along the horizontal centreline from the section 5 to 6. This streaming flow distribution can be ascribed to the evolving vortices shown by sections 5 and 6 of Fig.5(a-c). There are two strong counter-rotating vortices accompanied by another two relatively weak counter rotating vortices in the section 5 and they adjust to approximately-equal strengths in the section 6. The appearance of these vortices can be further ascribed to the formation of two counter-rotating vortices in the inhalation flow and four counter rotating vortices in the exhalation flow pertaining to the evolution of the instantaneous axial vorticity as shown in the section C4.

Along the core of the granddaughter branches, there is an exhalation streaming flow surrounded by an inhalation streaming. The inhalation streaming is stronger near the wall at the outside of the turn, similar to that in the secondary branches. The strength of both inhalation and exhalation streaming is highest near the bifurcation and gradually decreases away from the bifurcation as shown in sections 8 and 9 of Fig.4(a-c). The strength of the exhalation streaming in this region gradually decreases and spreads out along the plane passing through the centrelines of all branches by penetrating into the annular region of inhalation streaming. As evidently shown by Fig.5(a-c), this region comprises of 4 counter-rotating vortices near the bifurcation and rearranges to 2 clearly visible counter-rotating vortices away from the bifurcation. These 4 counter-rotating vortices appear as a consequence of

splitting 2 counter-rotating vortices of the intermediate branch subjected to the inhalation flow (see panel  $\phi = 0$  of Fig.18).

While there is evidently a strong streaming flow in the upper generations, this is not the case in the lower generations. Panel (d) of Fig.5 shows the case  ${}^8G_{10}$ , and it is clear that in this case the streaming is negligible. (Note that the color map range is  $10^3$  times smaller here).

These observations reveal the formation of longitudinal vortices. To further investigate this, Fig.6 shows the secondary velocity vector field  $\mathbf{U}_{tr}$  superposed on contours of the streaming velocity  $\bar{\mathbf{U}}_{ax}$  on corresponding sample planes in the mother, daughter and granddaughter branches. The figure clearly shows that the lobes of high  $\bar{\mathbf{U}}_{ax}$  coincide with recirculation regions in the secondary flow.

In order to quantify the magnitude of secondary (transverse) velocity  $\mathbf{U}_{tr}$  and compare it with the magnitude of velocity vector  $|\mathbf{U}|$ , Fig.7 shows them by dashed and solid lines respectively. The variation of these quantities are shown along the abscissa  $S$  among cases  ${}^0G_2$ ,  ${}^1G_3$ ,  ${}^2G_4$ ,  ${}^3G_5$  and  ${}^8G_{10}$  represented by *red*, *magenta*, *green*, *black* and *blue* lines respectively. The strength of  $\mathbf{U}_{tr}$  is proportional to the Reynolds number and hence the peak of the  $\mathbf{U}_{tr}$  is proportional to the peak of  $|\mathbf{U}|$ . As a common feature to all the cases, secondary velocity measured along the centerline of the mother branch remains negligible and gradually picks up in the bifurcating region (between mother and daughter branches) to arrive at a peak near the end of the bifurcating region. Then it decreases along the intermediate (daughter) branch and arrives at a smaller peak for cases  ${}^0G_2$ ,  ${}^1G_3$  and decreases with fluctuations.  $\mathbf{U}_{tr}$  reaches up to 75 % of  $|\mathbf{U}|$  for the highest Reynolds number case, i.e.  ${}^0G_2$ .

As depicted by Fig.7, the strength of the secondary flow is correlated with the strength of streaming and hence it can be considered as a proxy for the mean streaming phenomenon. This is because both the motion of the fluid in a perpendicular plane to the streamwise direction and the asymmetry between inhalation and exhalation are caused by nonlinear effects. A number of studies have reported the evolution of a secondary flow as an important feature influencing the gas mixing [46, 47].

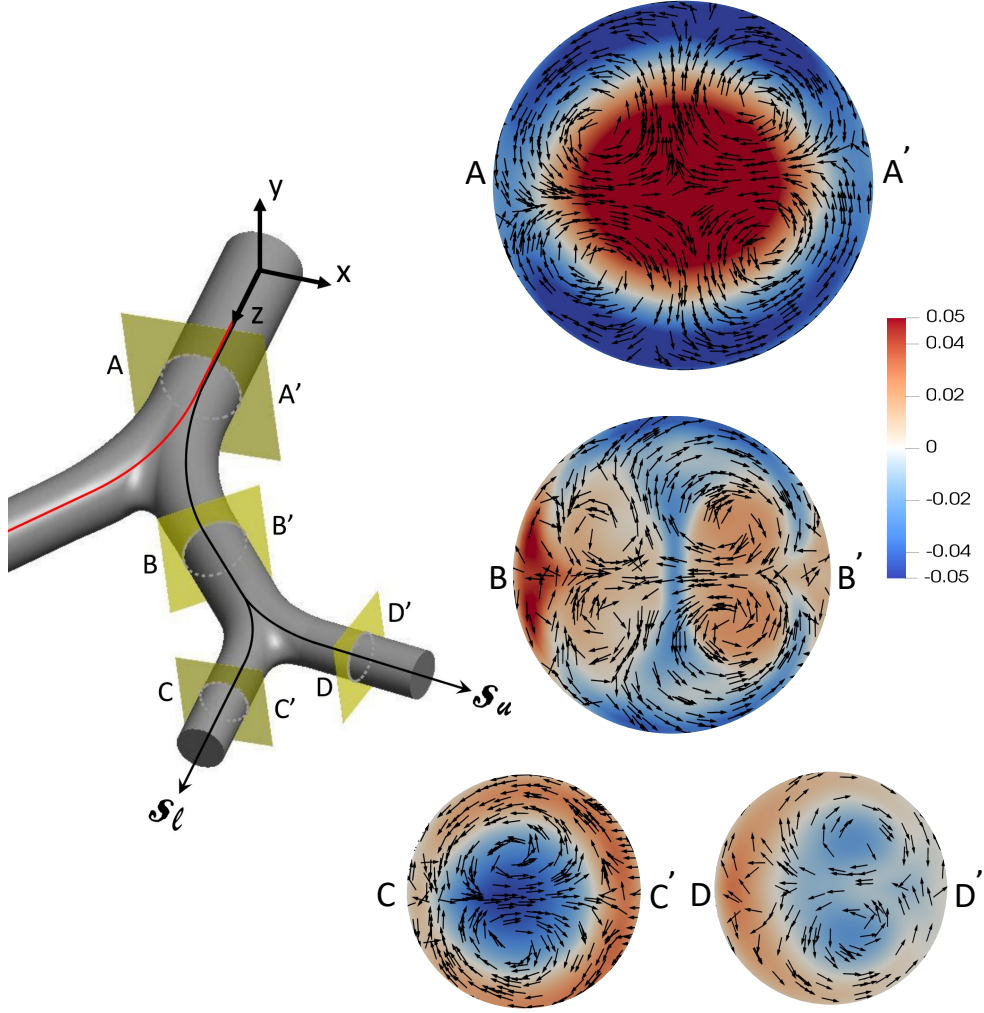


FIG. 6: Contours of dimensionless streaming velocity  $\bar{U}_{ax}/\hat{U}_{max}$  fields on cross sections A-A', B-B', C-C' and D-D' superposed with secondary flow vectors  $\mathbf{U}_{tr}$ . Note the vectors are uniform length, not scaled by magnitude, and so indicate the flow direction only. Cross sections A-A', B-B', C-C' and D-D' are located at the middle of the straight section at each generation level.

## 2. Recirculation

The previous sections have focused on a qualitative characterization of the streaming flow. In order to provide a quantitative portrait of this phenomenon, the amount of recirculating flux should be quantified which is indicative of the rate of gas transport via streaming in

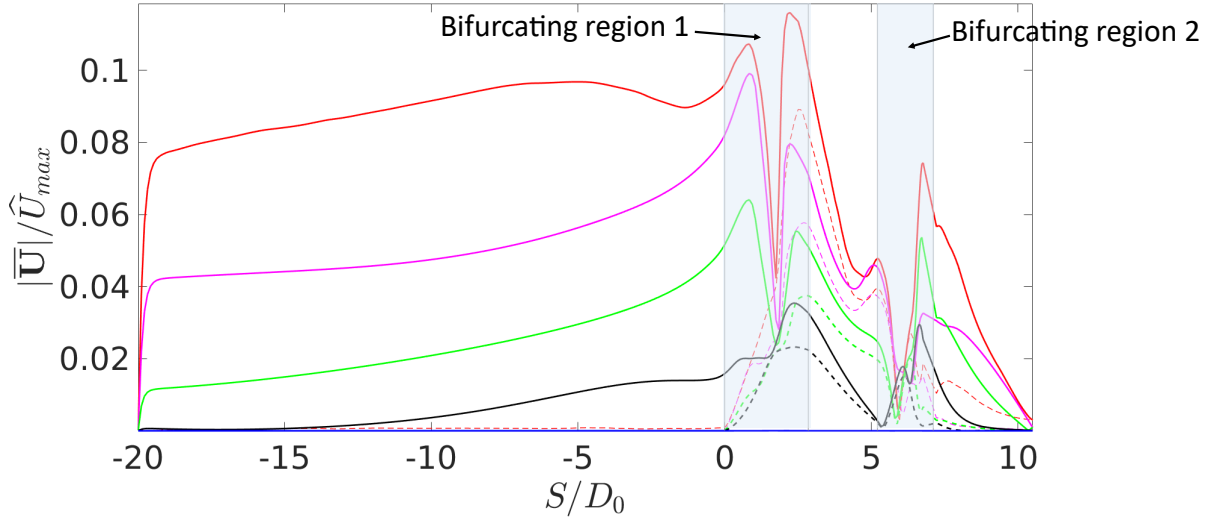


FIG. 7: Quantification of the magnitude of the secondary (transverse) velocity  $\mathbf{U}_{tr}$  and comparing it with the magnitude of the velocity vector  $|\mathbf{U}|$ .  $\mathbf{U}_{tr}$  and  $|\mathbf{U}|$  are indicated by dashed and solid lines respectively. The variation of these quantities are shown along the abscissa  $S$  among cases  ${}^0G_2$ ,  ${}^1G_3$ ,  ${}^2G_4$ ,  ${}^3G_5$  and  ${}^8G_{10}$  represented by *red*, *magenta*, *green*, *black* and *blue* lines respectively.

the airway. The amount of flow recirculated is quantified by using the positive flux of the cycle-averaged axial (streaming) velocity field  $\bar{\mathbf{U}}_{ax}$ . Essentially, over an arbitrary plane of interest, the flux over the portions where the flow is moving in one normal direction is equal and opposite to the flux over the portions where the flow is in the opposite normal direction. This is due to the fact that the overall mean flux must be zero across an arbitrary plane of interest. The amount of recirculating flux across a given plane of interest is computed by integrating the positive portions of velocity across the area normal to that positive velocity profile, given by

$$Q_r = \int_A \bar{\mathbf{U}}_{ax} \cdot \hat{\mathbf{n}} H(\bar{\mathbf{U}}_{ax} \cdot \hat{\mathbf{n}}) dA \quad (8)$$

where  $H$  is the Heaviside function and  $\mathbf{n}$  is the unit normal vector along the positive flow direction. This mean recirculating flux is then normalized by the maximum flow rate in the mother branch,  $Q_{max} = \pi D_0^2 \hat{U}_{max}/4$ . We performed the integration defined in equation 8 over a series of transverse planes to quantify  $Q_r$  as a function of the distance measured along

the computational domain.

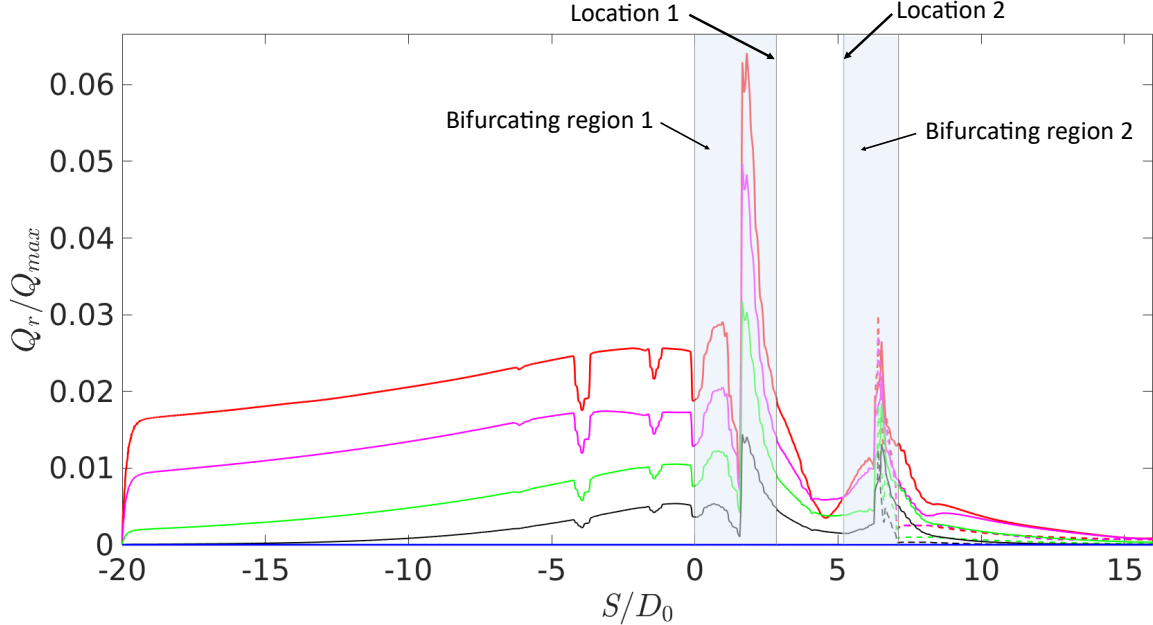


FIG. 8: Variation of recirculation flux  $Q_r$  along the entire flow domain for the cases among  ${}^0G_2$ ,  ${}^1G_3$ ,  ${}^2G_4$ ,  ${}^3G_5$  and  ${}^8G_{10}$  represented by *red*, *magenta*, *green*, *black* and *blue* solid lines respectively. The solid and dashed lines correspond to the recirculation flux measured in the lower and upper branches of the generation 2, and the shading represents the bifurcation region, i.e. the region where the centerlines are curved.

Figure 8 shows the variation of normalized recirculation flux as a function of distance measured along the computational domain in the cases modeling the first five intermediate generations, as well as the ninth generation. The solid and dashed lines correspond to the variation of recirculation flux measured along the lower and upper branches of the generation 2, i.e.  $S_l$  and  $S_u$ . Note that they are coincident up to the end of generation 1. The spatial location of the horizontal axis is presented in terms of distance measured along the abscissas  $S_u$  and  $S_l$  of the computational domain as defined in figure 2 and normalized by the diameter of the mother branch  $D_0$ . The shading represents bifurcating regions where the centerlines are curved. As clearly shown by Fig. 8, the basic pattern of spatial variation of the flux is the same in all four upper generation cases. They all display peaks of recirculation flux inside the bifurcation region and the value of the maximum peak is proportional to  $Re_{max}$ . As a common feature among upper generation cases, there are three troughs in the variation of recirculating flux within the region of  $-5D_0 < S < 0$  and the recirculation flux clearly

decreases along the intermediate branch before arriving at the second peak inside the next bifurcation.

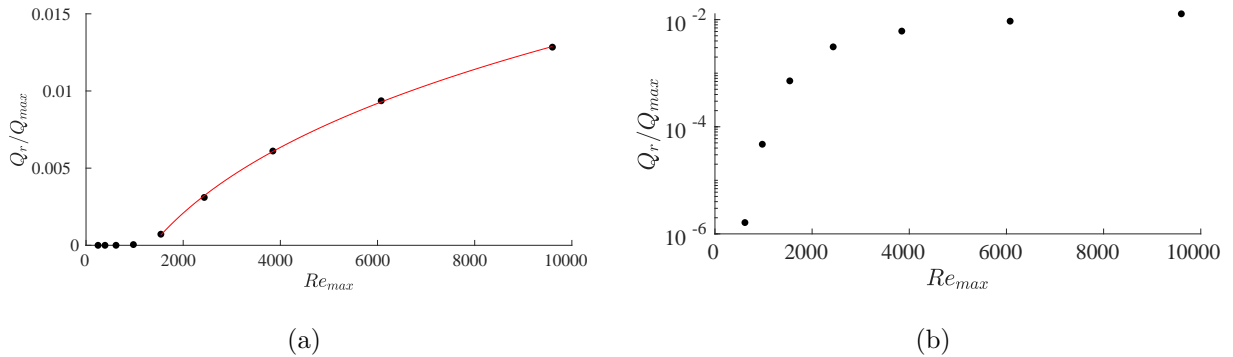


FIG. 9: Dimensionless recirculating flux computed at the borderline between the bifurcating region 1 and intermediate (daughter) branch as a function of  $Re_{max}$  for the first 9 intermediate generations modeling the airway. (a) The red curve shows a power law fit for the first 5 intermediate generations: :  $Q_r = Q_{max}[0.0034(Re_{max})^{0.25} - 0.02]$ . (b) The same data on a semilog scale, which shows the clear change in trend for generations below the fifth.

The most crucial measure of recirculation from the gas transport perspective is the amount of recirculation flux that passes on to the consecutive generation, as this allows gas to be passed from one generation to the next. In order to qualify mean streaming as a primary, or even significant, mechanism of gas transport in this context, the streaming needs to at least reach a few successive generation levels in the upper airway. If that is the case, the streaming flow is capable of transporting gas by virtue of a recirculation chain formed among these generation levels. Figure 8 shows the variation of normalized recirculation flux inside the intermediate generation ( $2.8D_0 < S < 5.2D_0$ ) bounded by bifurcating regions 1 and 2 (annotated in the figure), and neighbouring generations upstream and downstream. Noticeably, the value of  $Q_r$  at the borderline between the bifurcating region 1 and intermediate (daughter) branch is proportional to  $Re_{max}$ . In the simulation modeling the first generation of the airway, i.e.  ${}^0G_2$ , the recirculating flux measured at this location is around  $0.02Q_{max}$ , falling to around  $0.005Q_{max}$  for the fourth generation case  ${}^3G_5$ . By the ninth generation  ${}^8G_{10}$ , the recirculating flux is effectively zero.  $Q_r$  values measured at this location (the boundary between mother and daughter branch), pertinent to the first five generation

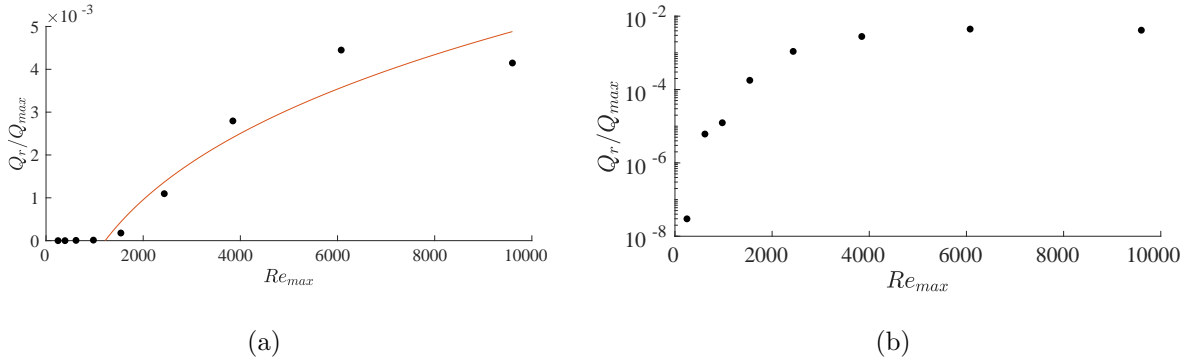


FIG. 10: Dimensionless recirculating flux computed at the borderline between the intermediate (daughter) branch and bifurcating regions 1 as a function of  $Re_{max}$  for the first 9 intermediate generations modeling the airway. (a) The red curve shows a power law fit for the first 5 intermediate generations:  $Q_r = Q_{max}[0.0012(Re_{max})^{0.25} - 0.0072]$ . (b) Semilog data of the first 9 intermediate generations.

levels varies like  $Re_{max}^{1/4}$  as shown in the Fig.9(a). The panel (b) of Fig.9 shows the same data but on a semilog scale to highlight the change in variation that occurs for generations lower than the fifth.

Similarly, the value of  $Q_r$  measured at the borderline between the intermediate (daughter) branch and bifurcating region 2, that is effectively the amount of recirculation flux passes on to the consecutive generation level as a function of  $Re_{max}$  is plotted in the Fig.10(a). Notably, the amount of recirculating flux that passes on to the consecutive generation level in the  ${}^1G_3$  case is slightly higher than that of the  ${}^0G_2$  case despite the fact that the highest  $Re_{max}$  is associated with the latter case.  $Q_r$  values measured at this location, pertinent to first five intermediate generation levels modeling the airway has been fitted in to a power law fit of  $Re_{max}^{1/4}$  as shown in the Fig.10. There is a local maximum in the dataset which is smoothed out by this fit, however, the fit still seems to capture most of the variation. Hereafter the borderline between the bifurcating region 1 and intermediate branch is referred as “location 1” and the borderline between the intermediate branch and bifurcating region 2 is referred as “location 2” for brevity.

The recirculating flux data presented in figures 9 and 10 can also be presented in terms of generation number. Figure 11 shows the effective strength of recirculating flux measured at the boundaries of each generation level over the first nine generations. *Blue* curves

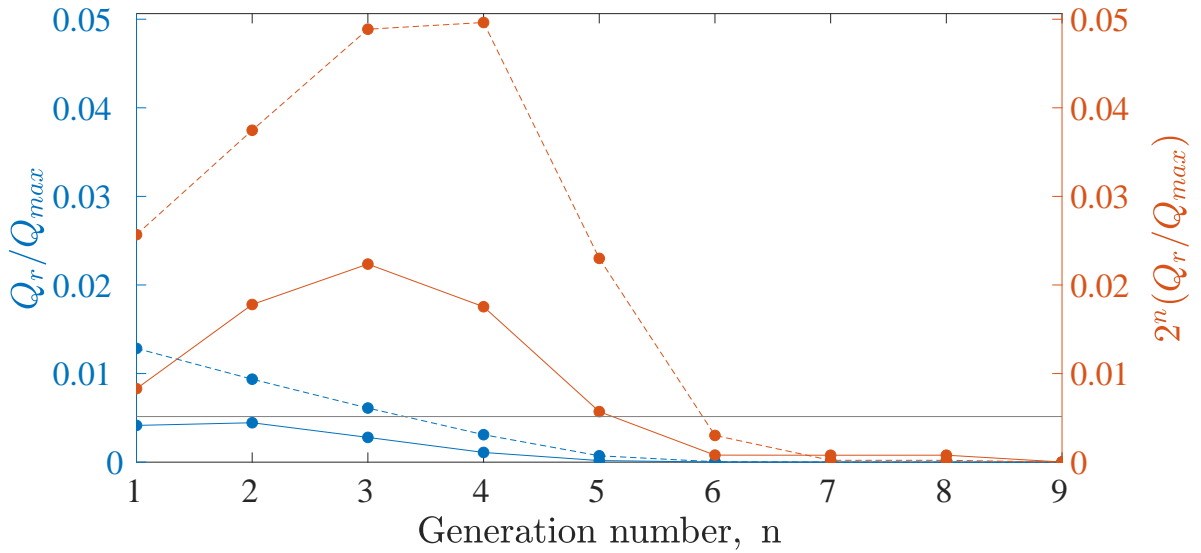


FIG. 11: Strength of the recirculating flux measured at the start and end of the intermediate generation level as a function of the generation number. *Blue* curves correspond to the strength of recirculating flux directly measured at a location of interest in the computational domain. *Orange* curves correspond to the total recirculating flux computed at each generation level. Dashed lines correspond to the measurements obtained at the borderline between the bifurcating region 1 and intermediate branch (location 1) and solid lines correspond to the measurements obtained at the borderline between the intermediate branch and bifurcating region 2 (location 2). The horizontal *gray* line corresponds to the flow rate required to meet the oxygen demand of a neonate in the clinical conditions based on the data reported by Hill and Robinson [48].

correspond to the strength of recirculating flux directly measured at a location of interest in the computational domain. *Orange* curves correspond to the total recirculating flux computed by multiplying the data in our computational domain - the *blue* curves - by a factor of  $2^n$  (where  $n$  is the generation number) which represents the number of airway vessels in each generation to compute the total recirculating flux at each generation level in the airway. Dashed lines correspond to the measurements obtained at the location 1 and solid lines correspond to the measurements obtained at the location 2.

As shown by the *orange* curves, the amount of recirculating flux measured at the location 1 is approximately twice that of location 2 for first six generations. This means the strength

of  $Q_r$  along a particular generation decreases by  $\sim 50\%$ .  $Q_r$  measured at location 1 increases from generation 1 to 4 to arrive at the highest in the generation 4, and gradually decreases in successive generations whereas  $Q_r$  measured at location 2 increases from generation 1 to 3 to arrive at the highest in the generation 3, and gradually decreases in successive generations. As a common feature for both variations,  $Q_r$  becomes negligible beyond the generation 6.

The role of this streaming recirculation from the clinical perspective of HFV can be assessed by comparing it to the oxygen requirement of a patient. Assuming a oxygen demand of  $7 \text{ ml kg}^{-1} \text{ min}^{-1}$  for a neonate in the clinical conditions as reported by Hill and Robinson [48], the amount of gas recirculation required to provide this can be calculated. This amount is marked by the horizontal gray line in figure 11. This comparison shows that the amount of oxygen passed on to the successive generation through the steady streaming phenomenon is potentially adequate to meet with the demand down to generation 5.

Figure 12 shows a comparison of the total recirculating flux between the multi-generation model and our previously reported study in a single-generation model (Jacob *et al.* [1]). *Blue* curves correspond to the  $Q_r$  measurements reported by Jacob *et al.* [1] (referred to as  $Q_{\text{sing}}$ ) and *orange* curves correspond to the  $Q_r$  measurements computed in this study (referred to as  $Q_{\text{mult}}$ ). Dashed lines correspond to the measurements obtained at the location 1 and solid lines correspond to the measurements obtained at the location 2. As a common feature of  $Q_r$  measurements obtained at both locations, i.e.  $Q_{r1}$  and  $Q_{r2}$ , the total recirculating flux reported in the single generation model is higher than that in the multi-generation model - the asymmetry between the inhalation and exhalation flow is less when longitudinal vortices are generated in both directions, and is an outcome of the coupling between generations. Notably, the peak value of  $Q_{r1}$  in the single generation model is observed at the generation 3 while that of the multi-generation model is observed at the generation 4. The value of  $Q_{r1}$  is reduced up to 40% with the coupling effects. Similarly, the peak value of  $Q_{r2}$  in the single generation model is observed at the generation 2 while that of the multi-generation model is observed at the generation 3. The value of  $Q_{r2}$  is reduced up to 63% with the coupling effects. Despite this reduction in magnitude, the generation to which the streaming is estimated to be able to provide gas exchange that is clinically relevant is similar between the two models.

Figure 11 clearly shows that the streaming can be a potential gas transport mechanism in the upper airway. Streaming can deliver gas over the distance into successive generations by virtue of a recirculation chain formed among generations. Here, we investigate this

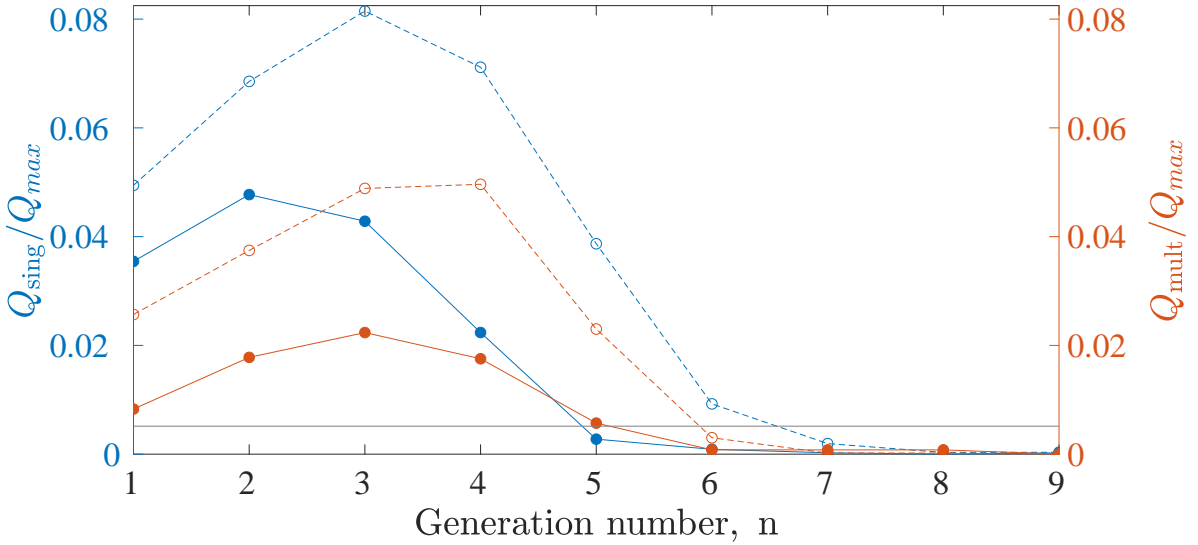


FIG. 12: Comparing the total recirculating flux computed in this study (as shown in the Fig.11) with that of our previous study (Jacob *et al.* [1]) pertinent to removed coupling between generations. *Blue* curves correspond to the  $Q_r$  measurements reported by Jacob *et al.* [1] (referred to as  $Q_{\text{sing}}$ ) and *orange* curves correspond to the  $Q_r$  measurements computed in this study (referred to as  $Q_{\text{mult}}$ ). Dashed lines correspond to the measurements obtained at the location 1 and solid lines correspond to the measurements obtained at the location 2. The horizontal *gray* line corresponds to the flow rate required to meet the oxygen demand of a neonate in the clinical conditions based on the data reported by Hill and Robinson [48].

recirculating distance further. Figure 13 shows a shear stress magnitude distribution,  $|\tau|_{\text{mean}}$  on the walls of the domain calculated from  $\bar{\mathbf{U}}$  for the  ${}^0G_2$ . Note that  $|\tau|_{\text{mean}}$  is not the mean stress, but is instead the stress calculated from the time-mean flow. This quantity should be zero on any segment of the geometry where there is no mean streaming. The magnitude of  $|\tau|_{\text{mean}}$  is high in the bifurcation region where the streaming flow is strongest, and it gradually decreases to zero along the daughter branches. It does not settle back to zero along the long mother branch section, with a significant shear stress extending all the way to the free end, indicating that a streaming flow is present even at distances of  $20D_0$  from the bifurcation.

To further quantify this, figure 14 shows the variation of  $\bar{\mathbf{U}}_{ax}$  measured along the abscissas

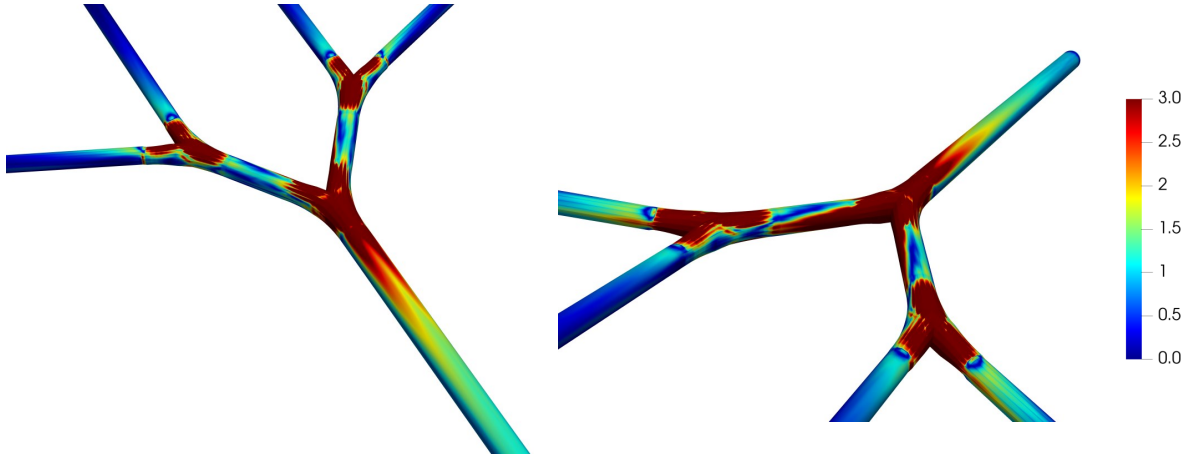


FIG. 13: Distribution of wall shear stress based on the streaming velocity field for  ${}^0G_2$   
 $(Re_{max} = 9600, \alpha = 3.36, L/a = 849)$ .

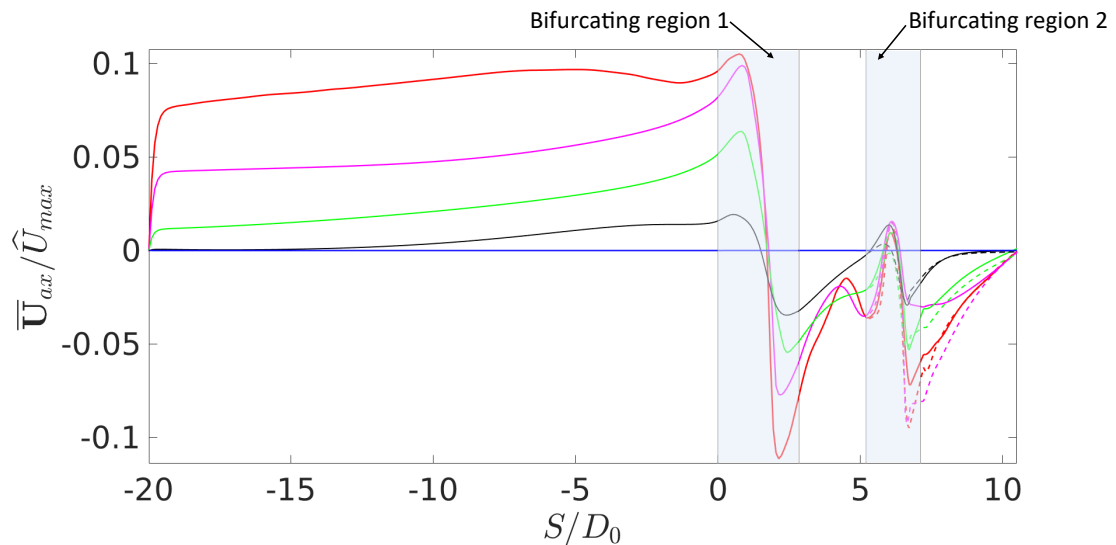


FIG. 14: Quantification of recirculation length  $L_r$  on the mother branch: variation of  $\bar{U}_{ax}$  measured along the abscissa  $S$  among  ${}^0G_2$ ,  ${}^1G_3$ ,  ${}^2G_4$ ,  ${}^3G_5$  and  ${}^8G_{10}$  represented by red, magenta, green, black and blue solid lines respectively.

$S_u$  and  $S_l$  of the computational domain for different generation cases. The variation of  $\bar{U}_{ax}$

along the abscissas  $S_u$  and  $S_l$  are shown by dashed and solid lines respectively. Abscissas  $S_u$  and  $S_l$  are identical from the mother branch up to the end of the intermediate generation and split beyond this point. Therefore,  $\bar{\mathbf{U}}_{ax}$  measured along abscissas  $S_u$  and  $S_l$  are identical up to the end of the intermediate generation and split afterwards. Figure 14 indicates that the  $\bar{\mathbf{U}}_{ax}$  field progressively weakens for each subsequent generation case, and becomes negligible by the  ${}^8G_{10}$  case. However, in all the generation cases  $\bar{\mathbf{U}}_{ax}$  passes through a local maximum at a distance around  $D_0$ , but then rapidly decreases to meet with a local minimum at around  $2D_0$  inside the bifurcating region 1. In  ${}^0G_2$  and  ${}^1G_3$  cases this is followed by a second local maximum, subsequently followed by fluctuations - in the other generations, this second local maximum is not observed and  $\bar{\mathbf{U}}_{ax}$  simply begins to increase after passing the minimum. Notable is the fact that  $\bar{\mathbf{U}}_{ax}$  gradually decays to zero beyond the bifurcating region 2 as a common feature to all the cases.

The results presented here link the gas transport capacity of the streaming flow to the strength of the Dean vortices formed. This suggests a potential strategy towards the optimization of HFV and low-volume ventilation methods - finding reciprocation variations that maximise the difference between the formation of Dean vortices during inhalation and exhalation may lead to a maximum efficiency of the streaming flow to transport gas. Driving the zero-net-mass-flux flow with an optimized frequency modulation setup to maximize the strength of the mean flow is a potential path to optimization.

### *3. Instantaneous events impacting the mean structure*

In section C1, it was argued that the features observed in the streaming flow (cycle-averaged velocity) field were driven by the presence of the longitudinal vortex system generated by Dean's mechanism. Here, we interrogate this argument by capturing the iso-surfaces of coherent structures associated with these vortical structures.

We further investigate the evolution of vortical structures characteristic to the flow to interpret the flow breaking down into turbulence. The  $\lambda_2$ -criterion [49] detects the pressure minimum to identify a coherent structure, based on an approximation to the pressure Hessian and obtaining eigenvalues. However, due this approximation of removing unsteady and viscous terms of the pressure Hessian, the small scales in the flow are filtered out leaving only the larger coherent structures.

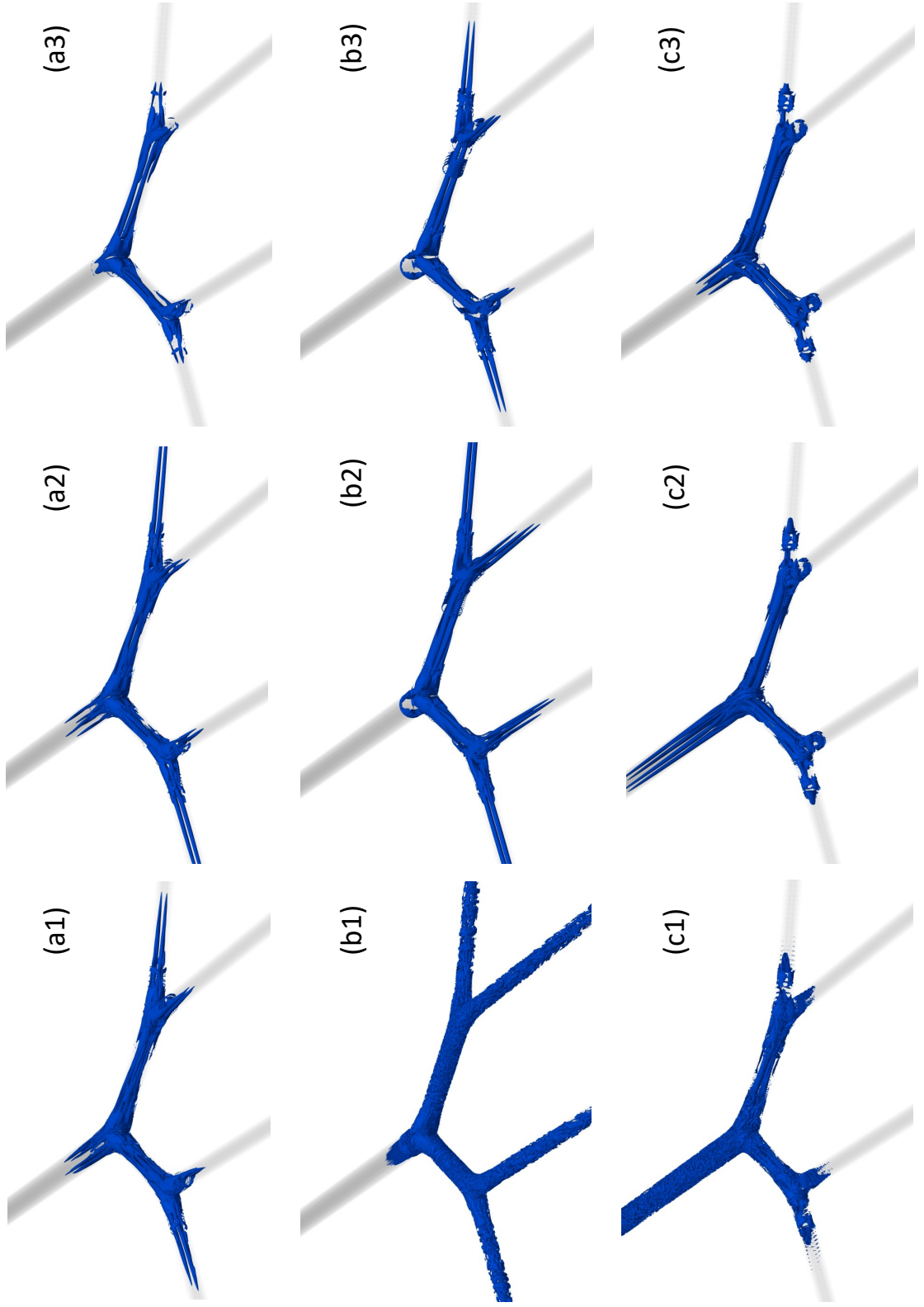


FIG. 15: Isosurfaces of  $\lambda_2$  vortical structures based on the threshold value of  $-0.0025$ . (a1), (a2) and (a3) correspond to iso-surfaces generated based on the streaming velocity field of  ${}^0G_2$ ,  ${}^1G_3$  and  ${}^2G_4$  cases respectively. Similarly, (b1), (b2) and (b3) correspond to iso-surfaces generated based on the peak inhalation flow field of  ${}^0G_2$ ,  ${}^1G_3$  and  ${}^2G_4$  cases respectively. Further, (c1), (c2) and (c3) correspond to iso-surfaces generated based on the peak exhalation flow field of  ${}^0G_2$ ,  ${}^1G_3$  and  ${}^2G_4$  cases respectively. The animation `lam_0G2.avi` provided in the supplementary material shows the evolution of isosurfaces of  $\lambda_2$  vortical structures pertinent to  ${}^0G_2$  case.

Figure 15 shows 9 panels of iso-surfaces of coherent structures generated based on the  $\lambda_2$ -criterion, which defines vortex cores as any region where  $\lambda_2 \leq 0$ . Each panel illustrates iso-surfaces of these vortical structures based on the threshold value of  $\lambda_2 = -0.0025$ . Three panels in the first row,  $a1, a2$  and  $a3$  correspond to iso-surfaces generated based on the streaming velocity field of  ${}^0G_2$ ,  ${}^1G_3$  and  ${}^2G_4$  cases respectively. Similarly, three panels in the second row,  $b1, b2$  and  $b3$  correspond to iso-surfaces generated based on the peak inhalation flow field of  ${}^0G_2$ ,  ${}^1G_3$  and  ${}^2G_4$  cases respectively. Further, three panels in the third row,  $c1, c2$  and  $c3$  correspond to iso-surfaces generated based on the peak exhalation flow field of  ${}^0G_2$ ,  ${}^1G_3$  and  ${}^2G_4$  cases respectively.

Pertaining to the first row of Fig.15, the streamwise vortical structures appear to be apparent in the panel (a2) than that of (a1). This indicates stronger vortical structures present in the  ${}^1G_3$  case in which no turbulence is observed than the  ${}^0G_2$  case in which conditional turbulence is observed. This phenomenon seems to be contradicting with the variation of recirculation flux  $Q_r$  (as demonstrated in Fig.8) where the strength of  $Q_r$  is higher in the case  ${}^0G_2$  than that of  ${}^1G_3$ . This suggests there is a process - conditional turbulence - that destroys the coherence of the mean vortex structures such that they are not reliably detected using the  $\lambda_2$  criterion.

Evidence of this process - the appearance of conditional turbulence growing on these streamwise vortex structures - is clear in the subsequent images in Fig.15. The second row of images shows the  $\lambda_2$  isosurfaces at peak inhalation. During the inhalation half-cycle, vortical structures progressively enlarge along each daughter and granddaughter branch along the flow direction, which can be ascribed to the centrifugal instability in the curved section of each bifurcation. These structures are clear in the images (b2) and (b3) for the  ${}^1G_3$  and  ${}^2G_4$  cases, respectively. However, the  ${}^0G_2$  case shows a much more complex structure, with the downstream of first bifurcation being filled with small-scale turbulent eddies.

A similar process occurs during exhalation. Again, two counter-rotating vortices are formed from the centrifugal instability induced by the curvature of the bifurcation where the flow is leaving each granddaughter branch. This results in two counter-rotating vortex pairs, or four streamwise vortices, entering each daughter branch. This four-vortex system is clearly apparent in the daughter branches as shown in the panel (c2) for the  ${}^1G_3$  case. Then this four-vortex system from each daughter branch enters in to the mother branch and becomes an eight-vortex system near the first bifurcation and rearranges to another four-

vortex system away from the bifurcation. However, the panel (c1) for the  ${}^0G_2$  case shows this structure breaking down into small-scale turbulent eddies that fill the entire mother branch.

The appearance of turbulence coincides with the break down of the streamwise vortex structures, and we conjecture that this turbulence occurs via an instability of this vortex system. This idea is consistent with the data and we investigate the onset of this turbulent structure and its potential mechanism of generation in the following sections.

#### *4. Instantaneous evolution of the velocity field*

Here, we investigate the evolution of the instantaneous velocity field  $\mathbf{u}(\mathbf{x}, t)$  over a complete flow cycle, especially in the upper airway that is susceptible for turbulence. Results are presented here at 12 instants and for clarity and conciseness of flow visualizations, only one half of the fluid domain is shown in each panel. These velocity fields were indeed verified to be statistically symmetric around the  $z$ -axis, reflecting the symmetry of the local geometry.

Figures 16 and 17 show contours of velocity magnitude  $|\mathbf{U}|$  for 12 consecutive phases of the cycle among cases  ${}^0G_2$  and  ${}^1G_3$ . The first and the last panels correspond to  $\phi = 0$  and  $\phi = \frac{11}{6}\pi$  respectively with an interval of phase angle  $\Delta\phi = \frac{\pi}{6}$  between each consecutive panel. The upper 6 panels of each figure corresponds to the inhalation half cycle while the lower 6 panels correspond to exhalation. As observed in Fig. 16 and 17, the streamwise velocity field is clearly a function of the inlet boundary condition.

For the  ${}^0G_2$  case, during the first quarter of the cycle (acceleration phase during which the inhalation flow rate increases with time), a high momentum region progressively develops in the core of the mother branch and propagates along the inner walls of the daughter branches. Simultaneously, slightly weaker high momentum regions evolve in the core of daughter branches and propagate downstream along the inner walls of the granddaughter branches. Near the bifurcating regions, these high momentum regions progressively contrast with the slower moving air at the outer wall. The stronger high momentum region developed at the inner walls of the daughter branches breaks down to turbulence, approximately from  $1.2D_1$  measured along the daughter branches (from the origin of the first bifurcation) when  $\phi = \pi/3$ . This turbulence rapidly convects downstream and appears to be sustained for  $\frac{\pi}{3} \leq \phi \leq \frac{2\pi}{3}$  as depicted from panels 3 – 5 of Fig. 16.

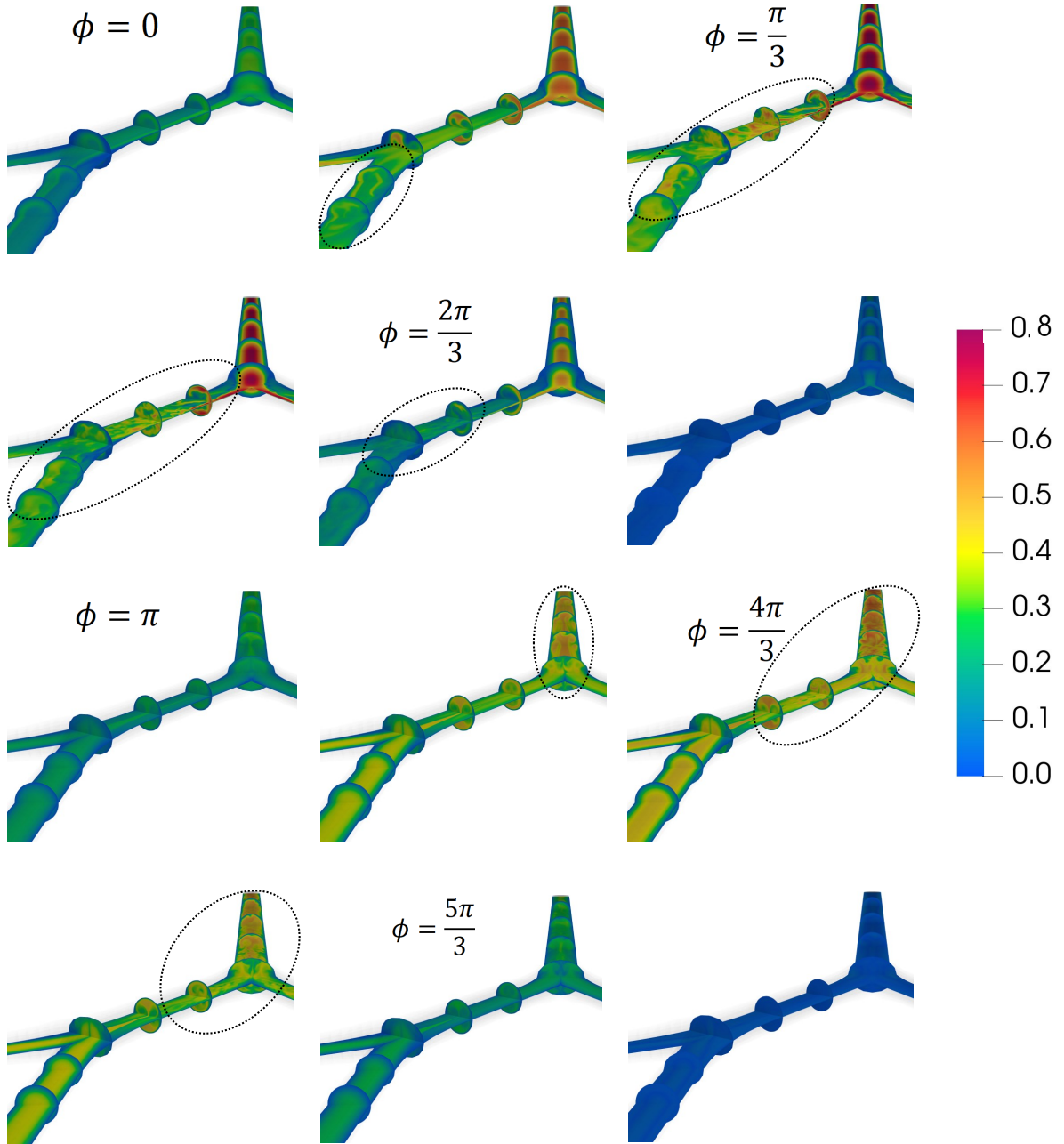


FIG. 16: Evolution of the instantaneous velocity magnitude,  $|\mathbf{U}|$  for  ${}^0G_2$  ( $Re_{max} = 9600$ ,  $\alpha = 3.36$ ,  $L/a = 849$ ). The dotted lines highlight areas where turbulent bursts have developed in the flow. The animation `vel_0G2.avi` provided in the supplementary material shows the evolution of  $|\mathbf{U}|$ .

In the second quarter of the cycle (deceleration phase during which the inhalation flow rate decreases with time), the turbulence decays when the flow velocity decreases below

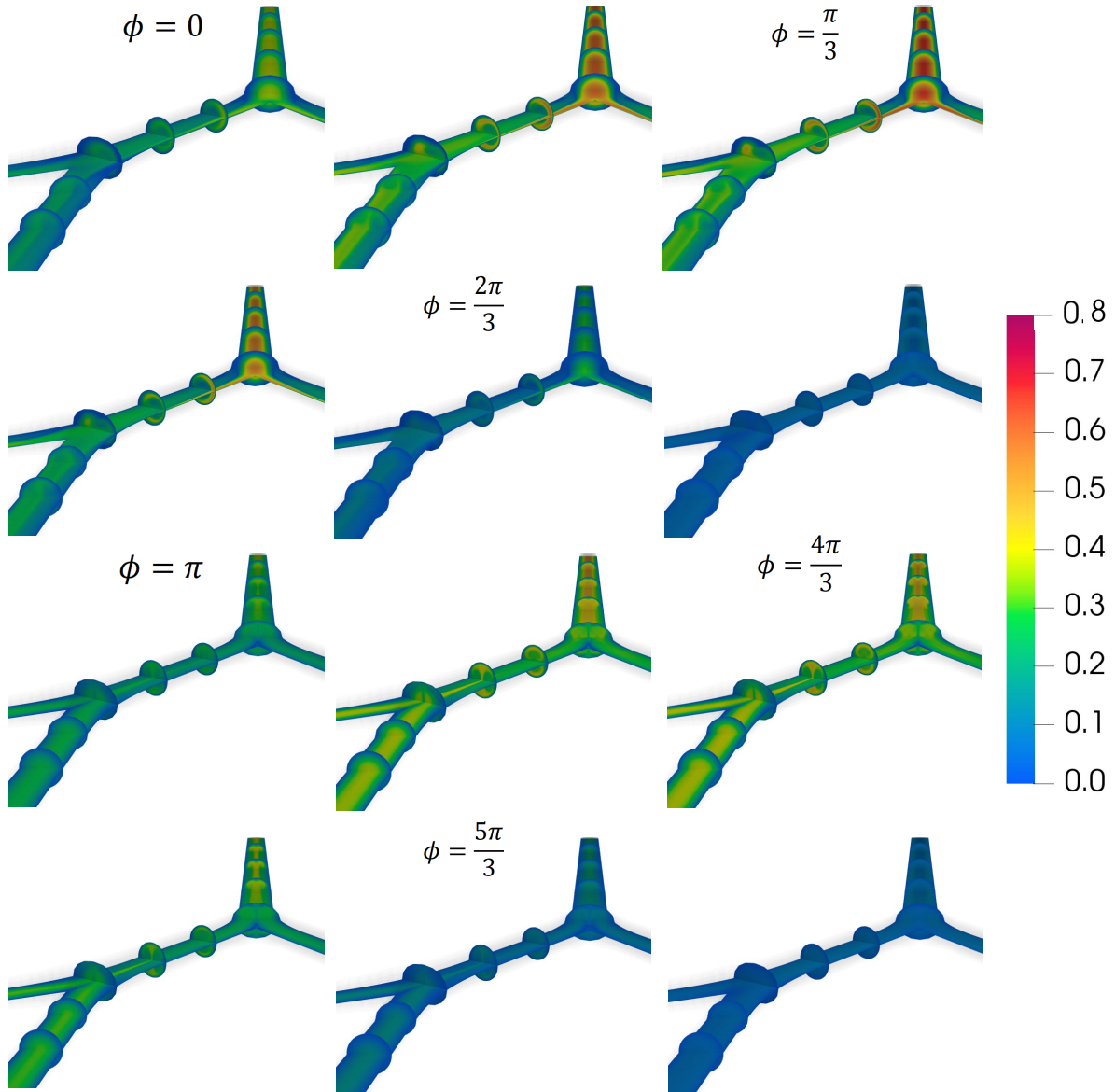


FIG. 17: Evolution of the instantaneous velocity magnitude,  $|\mathbf{U}|$  for  ${}^1G_3$  ( $Re_{max} = 6076$ ,  $\alpha = 2.66$ ,  $L/a = 861$ ).

a critical value. Eventually, the high momentum region depletes gradually and the flow relaminarizes as shown in panels 5 – 6. As shown by panel 6, the flow velocity decreases and alternates to facilitate the flow inversion between inhalation and exhalation phases.

In the third quarter of the cycle (acceleration phase during which the exhalation flow rate increases with time), the flow streams from granddaughter to daughter and daughter to mother branches. These flows merge to create jet-like high-momentum regions and these

high-momentum regions propagate along the core of the daughter and mother branches. As shown by the panel 8 of Fig. 16, the high-momentum region formed along the core of the mother branch breaks down to turbulence, approximately from  $5D_0$  measured along the mother branch. Simultaneously, jet-like high-momentum regions formed along the core of the daughter branches undergo an instability leading to periodic shedding of a structure that convects along the flow (this periodic pulsing is clear in the animation `vel_0G2.avi` provided in the supplementary material). This vortex shedding process repeats 15 times during an epoch around the peak exhalation flow rate and causes the generation of turbulence in the daughter branches. This turbulence, however does not sustain for a long time and disappears immediately once the shedded vortical structure is convected. The discrete nature of the flow instability generated here differentiates it from the classical fully developed turbulence.

In the final quarter of the cycle (deceleration phase during which the exhalation flow rate decreases with time), the turbulence decays in both daughter and mother branches and the flow relaminarizes while the high momentum region depletes gradually to facilitate the flow inversion for the next cycle.

A comparison of Fig.16 and 17 reveals that the corresponding cases  ${}^0G_2$  and  ${}^1G_3$  share qualitatively similar basic flow features except that there is no turbulence observed in the latter case.

Next we focus on the evolution of basic streamwise vortex structure influenced by the presence of turbulence for the  ${}^0G_2$  case. Figure 18 shows contours of axial vorticity  $\omega_{ax}$  at 12 instants of the flow cycle along 8 cross sections of the computational domain. The first and the last panel correspond to  $\phi = 0$  and  $\phi = \frac{11}{6}\pi$  respectively with an interval of phase angle  $\Delta\phi = \frac{\pi}{6}$  between each consecutive panel. The first 6 panels correspond to the inhalation half cycle while the next 6 panels correspond to exhalation.

According to the first 6 panels pertaining to inhalation, there is no apparent vortical structure observed in the mother branch due to the undisturbed nature of the flow. However, this undisturbed flow undergoes Dean's mechanism for the first time when the flow passes from mother to daughter branches and for the second time when the flow passes from daughter to granddaughter branches. As a consequence of the flow passing through the first bifurcation, there is a pair of counter-rotating vortices generated in the daughter branches which are symmetric around the  $x - z$  plane. When this flow (comprising of two counter-rotating vortices) passes through the second bifurcation, the single counter-rotating vortex

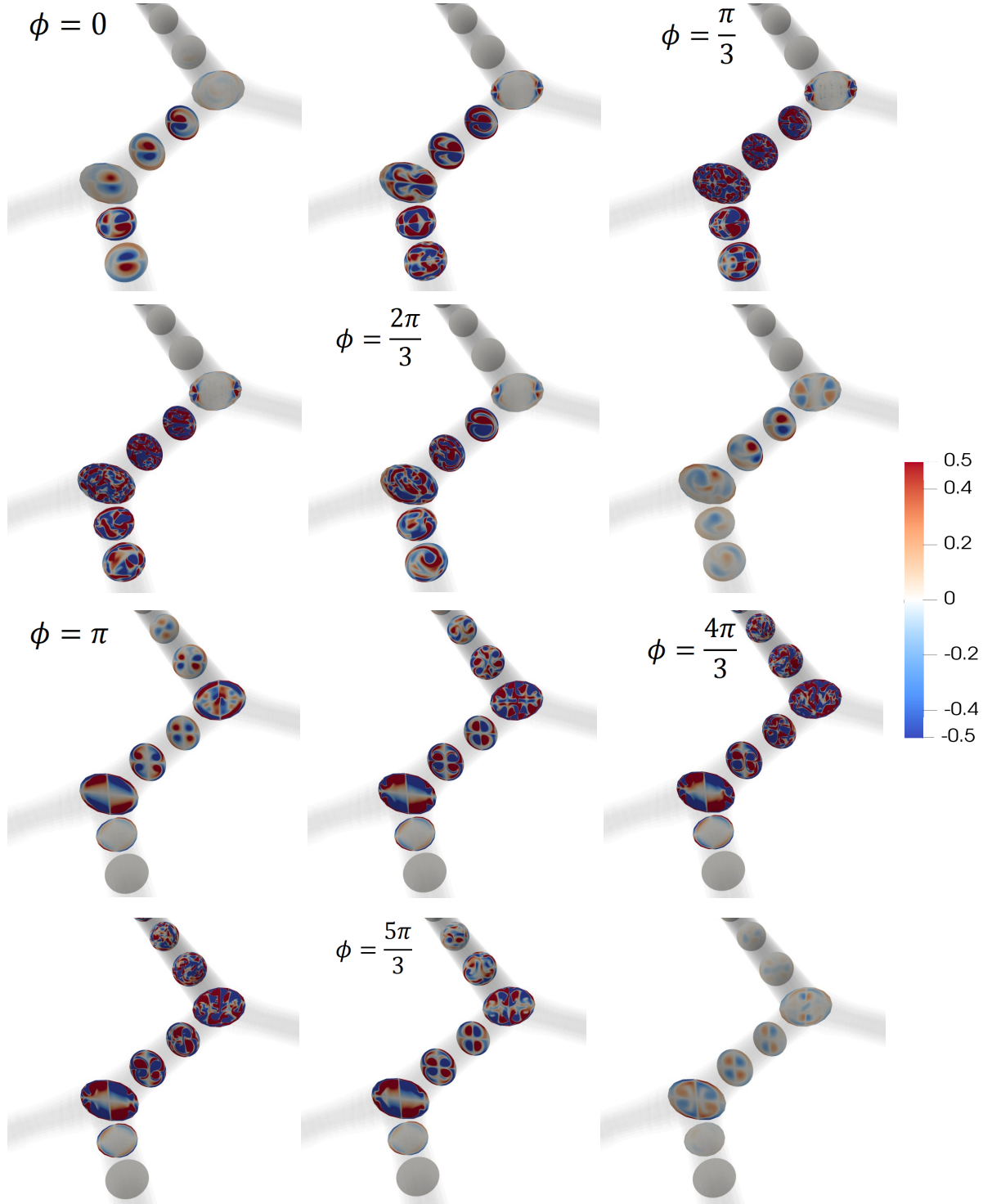


FIG. 18: Evolution of the axial vorticity  $\omega_{ax}$  for  ${}^0G_2$  ( $Re_{max} = 9600$ ,  $\alpha = 3.36$ ,  $L/a = 849$ ).

pair splits into two counter-rotating vortex pairs. These two counter-rotating vortex pairs rearrange back into a single counter-rotating vortex pair while alternating the direction

of rotation further away from the second bifurcation (note the symmetry of  $\omega_{ax}$  contours around the  $x-z$  plane where counter-clockwise and clockwise rotating vortices are observed. However, corresponding regions of the granddaughter branches are occupied by vortices rotating in the opposite direction). These vortical structures are then heavily distorted by the presence of turbulence during  $\pi/6 \leq \phi \geq \frac{2\pi}{3}$  before rearranging for the exhalation. During an epoch of flow inversion between inhalation and exhalation, these vortical structures seem to be rotated around the centerline of corresponding branches.

According to the last 6 panels pertaining to exhalation, there is no apparent vortical structure observed along the granddaughter branches due to the undisturbed nature of the flow when it passes from granddaughter, to daughter, to mother branches. This undisturbed flow undergoes Dean's mechanism for the first time when it passes from granddaughter to daughter branches and for the second time when it further passes from daughter to mother branches. As a consequence of the flow passing through the first bifurcation (when two branches merge together to form a single branch), there are two pairs of counter-rotating vortices generated in the intermediate (daughter) branches. When this flow (comprising of two counter-rotating vortex pairs) passes through the second bifurcation, the two pairs of counter-rotating vortices merge together to form four pairs of counter-rotating vortices. These four counter-rotating vortex pairs rearrange back into two counter-rotating vortex pairs further away from the mother branch. These vortical structures are then heavily distorted by the presence of turbulence during  $\frac{7\pi}{6} \leq \phi \geq \frac{5\pi}{3}$  before rearranging to facilitate the flow inversion for the next cycle.

A comparison of the basic streamwise vortex structure indicated here with the coherent vortical structures captured by the  $\lambda_2$ -criterion explains the variation of recirculating flux discussed in Sec. C 2. It suggests that the turbulence occurring in the upper airway does not have a noticeable impact on the mean streaming, as the mean velocity field has not been influenced by the turbulence (see Fig.15). This feature of the flow leads to an important result from a clinical point of view: the impact of mean streaming on HFV can be controlled by manipulating the input pressure waveform to maximize the vortex structure despite the appearance of turbulence.

## 5. Further details of conditional turbulence

In this section, the temporal and spatial evolution of the velocity field during a flow cycle is further investigated. The temporal evolution of the instantaneous velocity field in the upper airway is probed by recording the history of the axial velocity  $\mathbf{U}_{ax}$  at the geometric center of each generation (center of the cross sections A-A', B-B', C-C' and D-D' of Fig.6). Three curves are shown in each panel: the raw history of  $\mathbf{U}_{ax}$  is shown in black, the low-pass filtered  $\mathbf{U}_{ax}$  is shown in green and high-pass filtered  $\mathbf{U}_{ax}$  is shown in red, using a cut-off frequency of  $f_{thr}D_0/\hat{U}_{max} = 0.05$  (note the frequency of the cycle for  ${}^0G_2$  case is  $fD_0/\hat{U}_{max} = 2\alpha^2/(\pi Re_{max}) = 7.5 \times 10^{-4}$ ). This decomposition enables the quantification of the time duration for which turbulence prevails.

Figure 19 reveals the appearance of turbulent bursts in the mother branch, centered around an epoch of time where the exhalation flow rate is close to maximum; in the daughter branches, centered around an epoch of time where both the inhalation and exhalation flow rate is close to maximum and in the granddaughter branches, centered around an epoch of time where the inhalation flow rate is close to maximum. As reported by Jacob *et al.* [1], we revisit here that this is in contrast to the behavior in the reciprocating flow in a straight tube in which the turbulent bursts typically occur at epochs centered around the peak deceleration [31, 32]. This difference appears to be due to the presence of the Dean vortices in the bifurcating geometry, and their subsequent instability. However, a formal stability or sensitivity analysis is required to fully understand this process.

The spatio-temporal evolution of the turbulent bursts pertinent to the  ${}^0G_2$  case is further investigated by space-time diagrams shown in the Fig. 20. The color contours of panel (a), (b) and (c) represent space-time diagrams of the axial velocity ( $\mathbf{U}_{ax}$ ) measured along the abscissas  $S_l$ ,  $S_u$  and centerline of the intermediate (daughter) branch (note that the panels (a) and (b) contain this region but magnified here for clarity). The shading represents the bifurcation region, i.e., the region where the centerlines are curved. The plot shown at the right of each panel shows the spatially averaged velocity as a function of time; implemented as the inlet boundary condition; which is proportional to the time varying flow rate. Note that the raw  $\mathbf{U}_{ax}$  data is high-pass filtered in order to remove the effect of the base reciprocating flow, and then spatially filtered (low wavenumber components are removed) in order to eliminate any mean trend embedded in the flow.

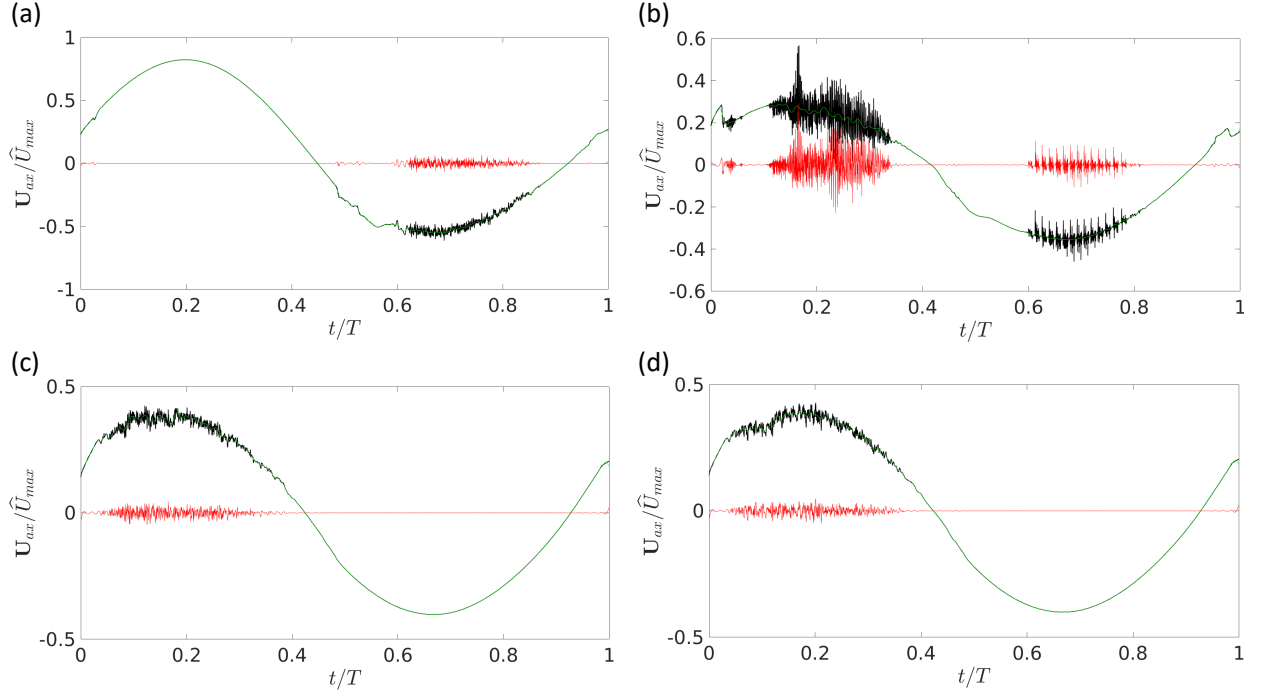


FIG. 19: A decomposition of the time history of axial velocity  $\mathbf{U}_{ax}$  of the  ${}^0G_2$  case. (a) Decomposition of temporal axial velocity ( $\mathbf{U}_{ax}$ ) at the center of the cross section A-A'. (b) Decomposition of temporal axial velocity ( $\mathbf{U}_{ax}$ ) at the center of the cross section B-B'. (c) Decomposition of temporal axial velocity ( $\mathbf{U}_{ax}$ ) at the center of the cross section C-C'. (d) Decomposition of temporal axial velocity ( $\mathbf{U}_{ax}$ ) at the center of the cross section D-D'. These cross sections are shown in Fig.6. Solid *black* line shows the measured temporal data from the instantaneous velocity field; solid *green* line shows the velocity scale associated with the filtered low-frequency components while the solid *red* line shows the velocity scale associated with the filtered high-frequency components. The cut-off frequency for the low- and high-pass filters was  $f_{thr}D_0/\hat{U}_{max} = 0.05$ .

Figure 20 reaffirms the fact that the turbulent bursts are centered around an epoch near the maximum flow rate. Further, it shows the spatial extent of these turbulent bursts. During an epoch near the peak inhalation, the extent of the fluid domain downstream of the first bifurcation is contaminated by fine-scale turbulent structures. During an epoch near the peak exhalation, convecting small-scale structures are observed throughout the domain, out of which the mother branch is filled with fine-scale turbulent structures and the daughter branches are filled with comparatively large-scale discrete convecting structures. Panels (a)

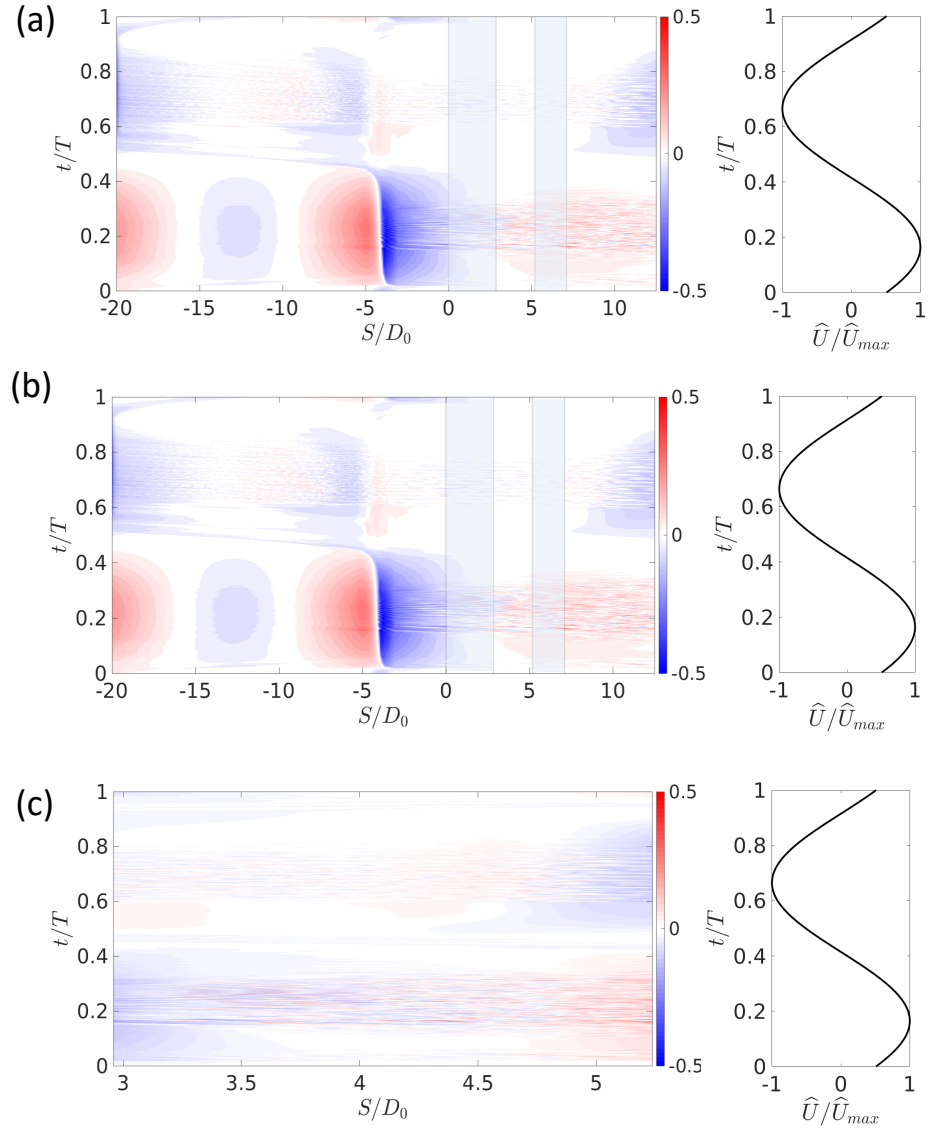


FIG. 20: Space-time diagram of spatially filtered (high wavenumber) and temporally filtered (high frequency) components of  $\mathbf{U}_{ax}$  for  ${}^0G_2$  ( $Re_{max} = 9600$ ,  $\alpha = 3.36$ ,  $L/a = 849$ ).  
 (a) Contours of filtered components of  $\mathbf{U}_{ax}$  plotted in the space-time coordinates along the abscissa  $S_l$ . (b) Contours of filtered components of  $\mathbf{U}_{ax}$  plotted in the space-time coordinates along the abscissa  $S_u$ . (c) Contours of filtered components of  $\mathbf{U}_{ax}$  along the magnified intermediate (daughter) branch. The shading represents the bifurcation region, i.e., the region where the centerlines are curved. The spatially averaged velocity as a function of time; implemented as the inlet boundary condition; which is proportional to the flow rate is shown at the right of each panel.

and (b) of the Fig. 20 display similar color contour distributions and essentially, they are identical from the free end of the mother branch up to the end of the intermediate generation ( $-20 \leq S/D_0 \geq 5.2$ ) as the abscissas  $S_u$  and  $S_l$  are coincident in this region. The upper and lower granddaughter branches share qualitatively similar color contour distributions of the space-time diagram, even though lower granddaughter branches were reported to have higher recirculation flux ( $Q_r$ ) distribution than that of the upper branches as revealed by Fig.8. The intermediate (daughter) branch region of the space-time diagram is magnified in the panel (c) to highlight the effects of both upstream and downstream coupling. As depicted from this visualization, the flow in the intermediate branch is contaminated by turbulent bursts near the peak flow rate of both inhalation and exhalation.

## *6. Effect of upstream and downstream conditions on the development of turbulence*

The previous sections have shown that the basic scenario for the appearance of conditional turbulence in the double bifurcation is similar to that uncovered in the single bifurcation reported in Jacob *et al.* [1], where turbulence occurs as a function of the local, and instantaneous, Reynolds number. However, the data of the present study allows this appearance to be studied in more detail by comparing flows with the same local and instantaneous parameters, but differing upstream and downstream conditions.

In this section, we therefore interrogate various simulation cases with equivalent local and instantaneous conditions, i.e., the same Reynolds and Womersley numbers, but different upstream and downstream conditions. For instance, the reciprocating flow through the lower bifurcating junctions of the  ${}^0G_2$  case (the two junctions between  $G_1$  and  $G_2$ ) shares the same local Reynolds number and Womersley number combination with the flow through the upper bifurcating junction of the  ${}^1G_3$  case (the junction between  $G_1$  and  $G_2$ ); however, they correspond to different upstream and downstream conditions.

In fact this comparison (lower junctions of the  ${}^0G_2$  case with the upper junction of the  ${}^1G_3$  case) can be made qualitatively from the flow visualisations of the  ${}^0G_2$  case in Figure 16 the  ${}^1G_3$  case in Figure 17 - it is clear that the flow characteristics during the inhalation are dependent on the upstream conditions. The lower bifurcating junctions of the  ${}^0G_2$  case see turbulent bursts during an epoch centered around peak inhalation flow rate, while the upper bifurcating junction of the  ${}^1G_3$  case does not see such bursts. Apparently, the production

of turbulence upstream is destabilising downstream and this turbulence is convected and sustained into the lower generations.

This observation is further quantitatively examined by plotting the temporal variation of axial velocity  $\mathbf{U}_{ax}$  of the  ${}^1G_3$  case in Fig. 21 sampled on the centreline in each generation. The locations of the sampling are provided in figure 6, and are in a geometrically similar position to those used for the sampled velocity data for the  ${}^0G_2$  case shown in figure 19.

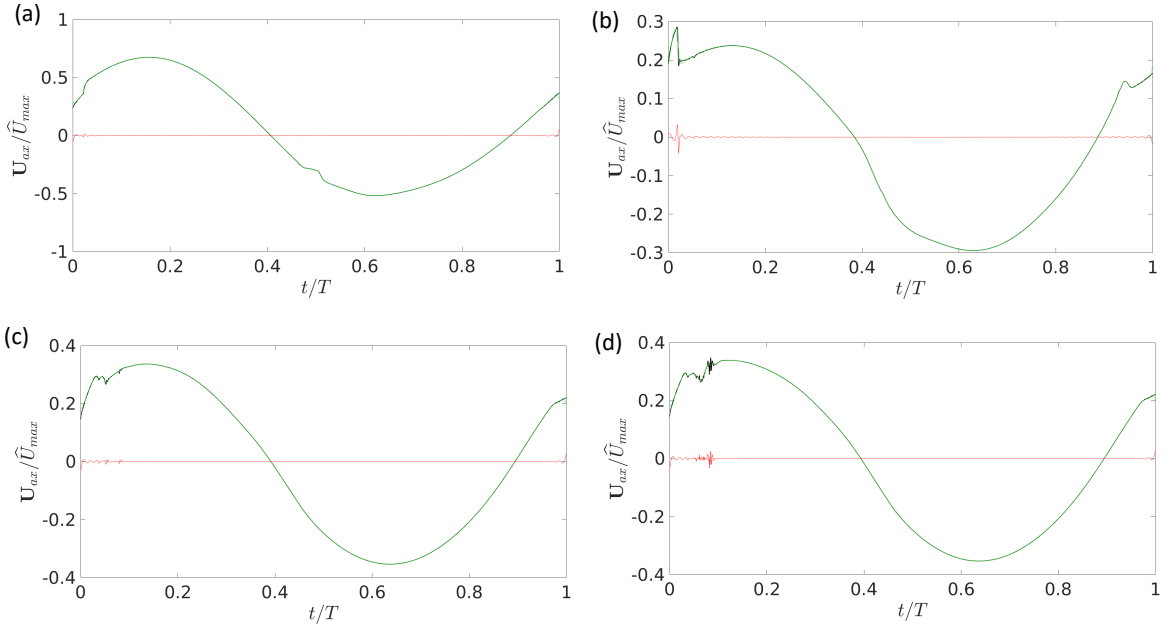


FIG. 21: A decomposition of the time history of axial velocity  $\mathbf{U}_{ax}$  of the  ${}^1G_3$  case. (a) Decomposition of temporal axial velocity ( $\mathbf{U}_{ax}$ ) at the center of the cross section A-A'. (b) Decomposition of temporal axial velocity ( $\mathbf{U}_{ax}$ ) at the center of the cross section B-B'. (c) Decomposition of temporal axial velocity ( $\mathbf{U}_{ax}$ ) at the center of the cross section C-C'. (d) Decomposition of temporal axial velocity ( $\mathbf{U}_{ax}$ ) at the center of the cross section D-D'. These cross sections are shown in Fig. 6. Solid *black* line shows the measured temporal data from the instantaneous velocity field; solid *green* line shows the velocity scale associated with the filtered low-frequency components while the solid *red* line shows the velocity scale associated with the filtered high-frequency components. The cut-off frequency for the low- and high-pass filters was  $f_{thr}D_0/\hat{U}_{max} = 0.05$ .

So, the sample location B-B', and the local Reynolds and Womersley number at this

location in the  ${}^0G_2$  case, are equivalent to location A-A' in the  ${}^1G_3$  case (the same equivalence occurs for C-C'/D-D' in the  ${}^0G_2$  case and B-B' in the  ${}^1G_3$  case). Therefore, panels (b) and (d) of Fig. 19 can be compared to panels (a) and (b) of Fig. 21 - the data have been sampled at geometrically similar locations, and the bulk flow conditions are also similar. Such a comparison reveals significant differences in the time history of axial velocity  $\mathbf{U}_{ax}$  which can be ascribed to the differences in upstream *and* downstream conditions among these cases.

The impact of this coupling between upstream and downstream generations is further investigated by comparing the cases described above to the flow in an isolated 1:2 bifurcation which by design removes the intergeneration coupling. Again, geometric and bulk dynamic similarity is maintained. Further, the computational mesh of each bifurcation employed is identical - the multigeneration meshes are constructed by connecting single generation meshes, thereby removing mesh dependence as a reason for any difference between the results from each simulation. The corresponding temporal evolution of axial velocity  $\mathbf{U}_{ax}$  is shown in Fig. 22.

The velocity traces produced are different to those from the multigeneration simulations shown in figures 19 and 21 for both the inhalation and exhalation flow. For example, figures 19(b) with the lower left panel of figure 22 compare the velocity trace in vessel generation 1 (the vessel beyond the first bifurcation) for the multi-generation and single generation cases respectively, with the same Reynolds and Womersley numbers in the mother branch. During inhalation, the only difference is the conditions downstream of the measurement point - the multi-generation mesh has another bifurcation, the single generation mesh has a long straight section. The velocity trace over the inhalation period ( $t/T < 0.5$ ) is similar in that turbulence occurs near the peak flow rate, however the amplitude of this turbulent fluctuation is clearly larger in the multi-generation case.

An important conclusion of this comparison is that it is not only *upstream* conditions that impact the production of turbulence; *downstream* conditions also need to be considered. We also highlight that the upstream and downstream directions reverse as the cycle moves from inhalation to exhalation.

This dependence on upstream and downstream conditions is further highlighted by visualizing the flow passing through each vessel generation for various setups. The evolution of the instantaneous velocity magnitude,  $|\mathbf{U}|$  among cases with equal Reynolds and Womersley numbers is shown in Fig. 23. Rows (a1) and (a2) of subfigure (a) correspond to cross sec-

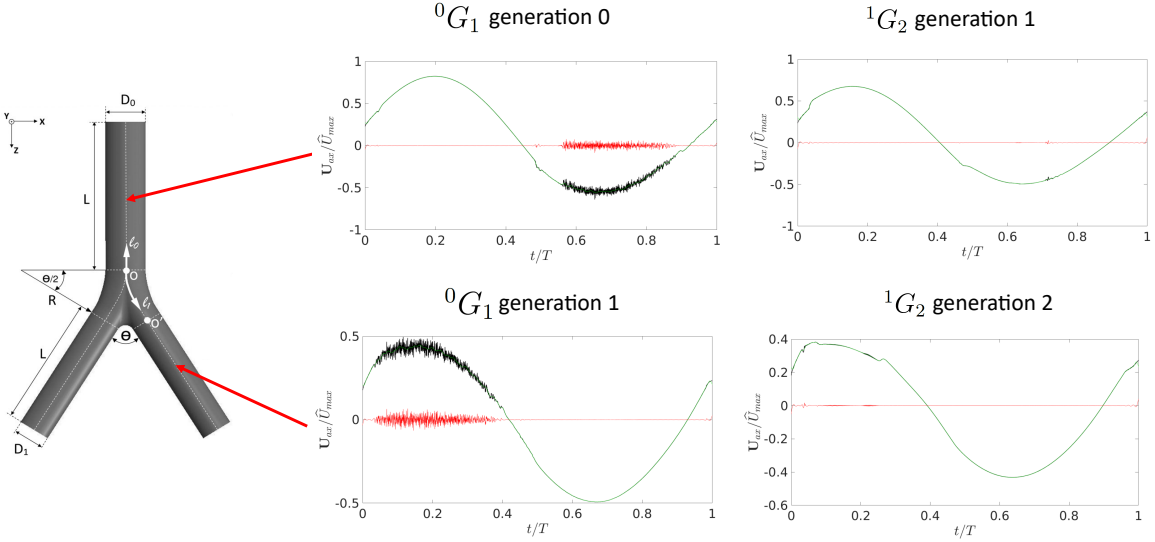


FIG. 22: A decomposition of the time history of axial velocity  $\mathbf{U}_{ax}$  of  ${}^0G_1$  and  ${}^1G_2$  cases. ( ${}^0G_1$  generation 0): Decomposition of  $\mathbf{U}_{ax}$  at the geometric center of the mother branch of  ${}^0G_1$  case. ( ${}^0G_1$  generation 1): Decomposition of  $\mathbf{U}_{ax}$  at the geometric center of a daughter branch of  ${}^0G_1$  case. ( ${}^1G_2$  generation 1): Decomposition of  $\mathbf{U}_{ax}$  at the geometric center of the mother branch of  ${}^1G_2$  case. ( ${}^1G_2$  generation 2): Decomposition of  $\mathbf{U}_{ax}$  at the geometric center of a daughter branch of  ${}^1G_2$  case. Solid *black* line shows the measured temporal data from the instantaneous velocity field; solid *green* line shows the velocity scale associated with the filtered low-frequency components while the solid *red* line shows the velocity scale associated with the filtered high-frequency components. The cut-off frequency for the low- and high-pass filters was  $f_{thr}D_0/\hat{U}_{max} = 0.05$ .

tions located at the geometric center of the mother branch of  ${}^1G_2$  case and the left daughter branch (section B-B' of Fig.6) of  ${}^0G_2$  case respectively. Rows (b1) and (b2) of subfigure (b) correspond to the left daughter branch of  ${}^1G_2$  case and the upper left granddaughter branch (section D-D' of Fig.6) of  ${}^0G_1$  case respectively. Each row contains 12 consecutive phases of the cycle and the first and the last panels correspond to  $\phi = 0$  and  $\phi = \frac{11}{6}\pi$  respectively with an interval of phase angle  $\Delta\phi = \frac{\pi}{6}$  between each consecutive panel. The first 6 panels of each row corresponds to the inhalation half cycle while the second 6 panels correspond to exhalation.

Row (a1) shows images from the first (mother) generation vessel of a single generation  ${}^1G_2$  case, whereas row (a2) are taken from the intermediate generation vessel of a multigeneration

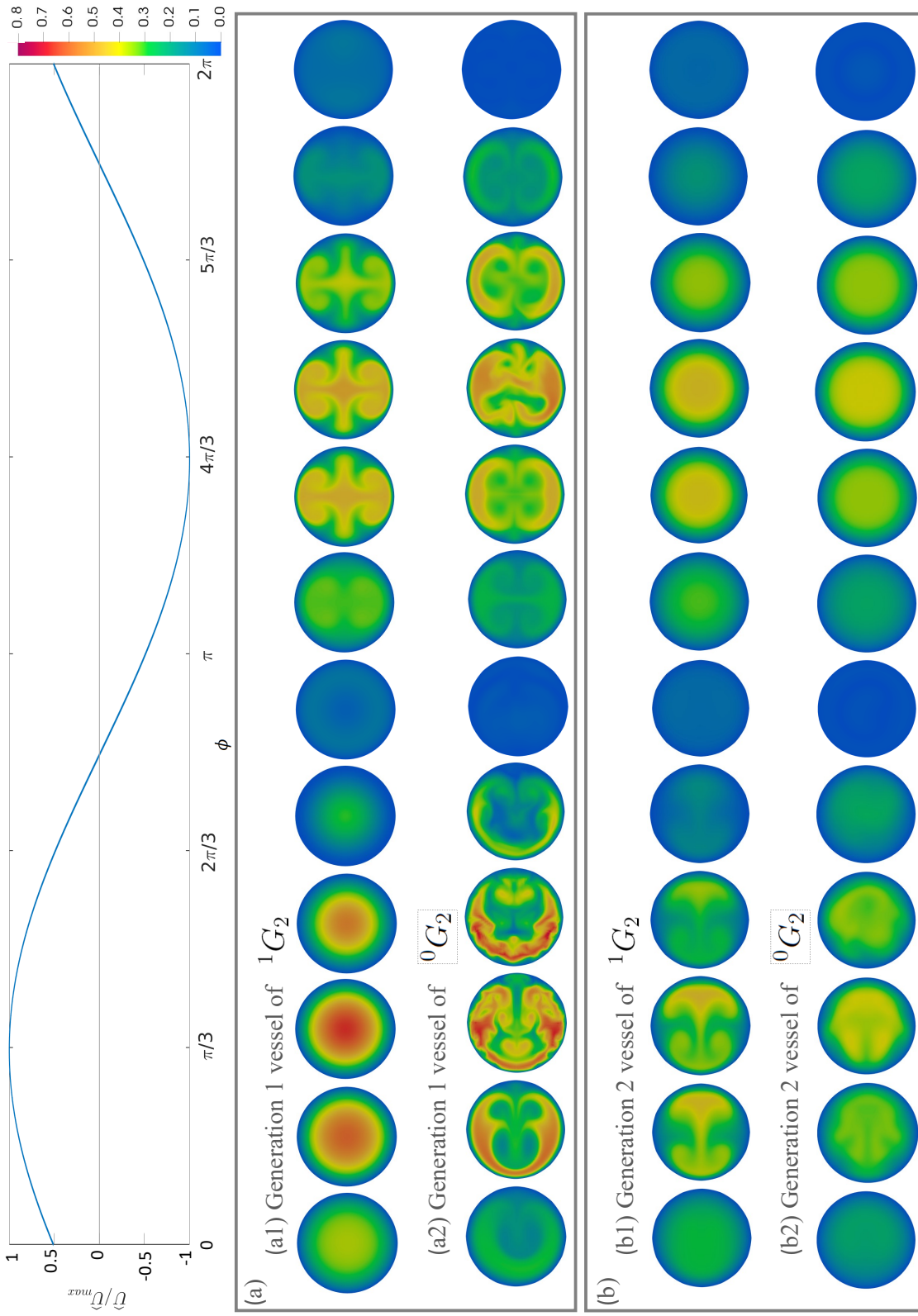


FIG. 23: A comparison of the evolution of the instantaneous velocity magnitude,  $|\mathbf{U}|$  among dynamically equivalent flow configurations. Rows (a1), (a2), (b1) and (b2) display 12 snapshots of  $|\mathbf{U}|$  at cross sections located at the geometric center of the mother branch of  $^1G_2$  case, the left daughter branch (section B-B' of Fig.6) of  $^0G_2$  case, the left daughter branch of  $^1G_2$  case and the upper left granddaughter branch (section D-D' of Fig.6) of  $^0G_1$  case respectively. Note that the diameter of daughter and granddaughter branches are scaled up by a factor of 0.79 and 0.79<sup>2</sup> to make them identical for comparison purposes. The top panel shows the variation of flow rate as a function of time.

${}^0G_2$  case.

The upstream conditions during the inhalation period (shown in the first 6 images of rows (a1) and (a2)) differ. The flow in the multigeneration case has already passed through a bifurcation, generating Dean vortices that subsequently become turbulent. The flow in the single generation case has only traversed the straight pipe section and presents an axisymmetric velocity profile. This strong modification by the upstream curvature is not surprising.

The comparison of the exhalation period (shown in the second 6 images of rows (a1) and (a2)) is less intuitive. During this exhalation period, the flow in the vessel shown is supplied by a flow that has passed through one bifurcation. All that changes is the downstream conditions - in the multigeneration case the vessel merges with another through a second bifurcation, whereas in the single generation case the vessel continues in a straight path. The images show there is a significant difference in the flow generated. Notably the multigeneration case displays a turbulent (or at least a spatiotemporally complex) flow when the flow rate is maximum near  $\phi = 4\pi/3$ , whereas the single generation case shows well-defined vortices throughout the exhalation period. The apparent conclusion is that the development of turbulence in this vessel is linked to the change in downstream conditions.

Rows (b1) and (b2) show the flow at a location in the vessel at generation 2: row (b1) shows a cross-section in the daughter branch of the single generation  ${}^1G_2$  case, whereas row (b2) shows a cross-section in the granddaughter branch of the multigeneration  ${}^0G_2$  case.

The first 6 panels of rows (b1) and (b2) correspond to inhalation, and so the upstream conditions between the two cases vary. Again, the flows are somewhat different to each other - the combined effects of curvature and flow division at multiple bifurcating junctions in the multigeneration case accumulate. The Dean vortices produced in the vessel at generation 1 have some impact on the Dean vortices produced in the vessel at generation 2, however the basic flow structure still appears to be dictated by these Dean vortices.

The second 6 panels of rows (b1) and (b2) correspond to exhalation, so that only the downstream conditions vary. The flows generated in this case are qualitatively similar, the axisymmetric velocity profiles generated through the straight inlet section of pipe do not appear to be impacted by the downstream conditions.

Taken together, one intuitive conclusion is that the development of turbulence is a strong function of the upstream conditions. Considering the fact that a preceding bifurcation generates a flow containing Dean vortices and a strong secondary flow (i.e, the flow normal

to the axis of the vessel), whereas the flow in a straight section is purely parallel, this outcome is not surprising.

What is less intuitive is the dependence on downstream conditions that is not universal - for example, the comparison of the exhalation flow in the vessel at generation 2 showed no dependence on upstream conditions during exhalation, whereas the flow in the vessel at generation 1 does show a dependence. This is possibly linked to the flow being supplied - the flow compared in generation 2 is essentially axisymmetric, whereas that compared at generation 1 contains Dean vortices. It is possible that the deficit produced by the Dean vortices and secondary flow provide a feedback mechanism, allowing the disturbance to the flow introduced by the second downstream bifurcation to be communicated upstream and therefore destabilise the flow. Such a feedback mechanism is not present in the purely parallel flow.

A more formal stability and sensitivity analysis of the flow is required to completely establish this link which we will pursue in a future study. What is clear is that the generation of turbulence in the airway is not a completely “local” phenomenon, and that generational coupling needs to be considered if the impact of turbulence is to be understood.

#### D. CONCLUSION

The aim of the present investigation is to quantify the role of nonlinear mean streaming in the context of HFV, while reporting characteristic features of the reciprocating flow. We expand on the previous study reported by Jacob *et al.* [1] in which coupling effects were deliberately removed to focus on the generic flow features emanating from a 1:2 bifurcation. Here we focus on quantifying the effect of coupling between generations by exploiting a 1:2:4 bifurcation geometry securing the self-similar properties used by Jacob *et al.* [1] and complying with their simulation cases. We provide a direct comparison of these studies while providing insights to the existing clinical procedures of HFV.

In the context of nonlinear mean streaming pertaining to the gas transport during HFV, Jacob *et al.* [1] reported that the recirculating flux can be up to  $\sim 5\%$  of the maximum flow rate in the trachea and primary bronchi. However, The present study reveals that the recirculating flux due to mean streaming up to around 2% of the maximum flow rate, which is less than the  $\sim 5\%$  reported in the single bifurcation. The reduction can be ascribed

to the intergeneration coupling effects. However, these results suggest that the amount of oxygen supplied through this phenomenon likely meets the anticipated oxygen demand of a neonate in the first 5 generations of the airway. In this context, there should be other highly efficient mechanisms active in the middle and lower parts of the airway.

As an important feature of the reciprocating flow, turbulent bursts are observed in the first 3 generations of the airway when the flow speed exceeds a critical value. The flow relaminarizes periodically when the flow speed decreases below the critical value. However, the results of this paper show that this critical value is a function of the geometry. The onset, advection and sustenance of turbulence in a given vessel appears to be a function of the upstream and downstream flow conditions. Multiple generations of the airway must be considered to fully understand this phenomenon.

## ACKNOWLEDGMENTS

CJ acknowledges the joint financial support of Swinburne University of Technology and the Murdoch Children's Research Institute via the growth SUPRA scheme. This work was performed on the Gadi national facility at NCI and OzSTAR national facility at Swinburne University of Technology. OzSTAR is funded by Swinburne University of Technology and the National Collaborative Research Infrastructure Strategy (NCRIS). DGT is supported by a National Health and Medical Research Council Career Development Fellowship (1123859) and the Victorian Government Operational Infrastructure Support Program.

- 
- [1] C. Jacob, D. G. Tingay, and J. S. Leontini, The impact of steady streaming and conditional turbulence on gas transport during high-frequency ventilation, *Theoretical and Computational Fluid Dynamics* **35**, 265 (2021).
  - [2] T. Standiford and M. Morganroth, High-frequency ventilation, *Chest* **96**, 1380 (1989).
  - [3] K. Bauer, E. Nof, and J. Sznitman, Revisiting high-frequency oscillatory ventilation in vitro and in silico in neonatal conductive airways, *Clinical Biomechanics* **66**, 50 (2019).
  - [4] The top 10 causes of death, <https://www.who.int/news-room/fact-sheets/detail/the-top-10-causes-of-death>, accessed: 2021-07-13.
  - [5] D. Prabhakaran, S. Anand, D. Watkins, T. Gaziano, Y. Wu, J. C. Mbanya, R. Nugent,

- V. S. Ajay, A. Afshin, A. Adler, *et al.*, Cardiovascular, respiratory, and related disorders: key messages from disease control priorities, *The Lancet* **391**, 1224 (2018).
- [6] J. J. Murray, A. Guha, and A. Bond, Overview of the development of heat exchangers for use in air-breathing propulsion pre-coolers, *Acta astronautica* **41**, 723 (1997).
  - [7] T. Pedley, Pulmonary fluid dynamics, *Annual Review of Fluid Mechanics* **9**, 229 (1977).
  - [8] J. Grotberg, Pulmonary flow and transport phenomena, *Annual Review of Fluid Mechanics* **26**, 529 (1994).
  - [9] A. Guha, Transport and deposition of particles in turbulent and laminar flow, *Annu. Rev. Fluid Mech.* **40**, 311 (2008).
  - [10] Z. Zhang and C. Kleinstreuer, Transient airflow structures and particle transport in a sequentially branching lung airway model, *Physics of Fluids* **14**, 862 (2002).
  - [11] D. Jan, A. Shapiro, and R. Kamm, Some features of oscillatory flow in a model bifurcation, *Journal of Applied Physiology* **67**, 147 (1989).
  - [12] K. Avila, D. Moxey, A. de Lozar, M. Avila, D. Barkley, and B. Hof, The onset of turbulence in pipe flow, *Science* **333**, 192 (2011).
  - [13] B. Eckhardt, T. Schneider, B. Hof, and J. Westerweel, Turbulence transition in pipe flow, *Annual Review of Fluid Mechanics* **39**, 447 (2007).
  - [14] H. Schlichting and J. Kestin, *Boundary layer theory*, Vol. 121 (Springer, 1961).
  - [15] C. K. Batchelor and G. Batchelor, *An introduction to fluid dynamics* (Cambridge university press, 2000).
  - [16] H. Chang, Mechanisms of gas transport during ventilation by high-frequency oscillation, *Journal of Applied Physiology* **56**, 553 (1984).
  - [17] H. Luo and Y. Liu, Modeling the bifurcating flow in a ct-scanned human lung airway, *Journal of Biomechanics* **41**, 2681 (2008).
  - [18] A. Banko, F. Coletti, D. Schiavazzi, C. Elkins, and J. Eaton, Three-dimensional inspiratory flow in the upper and central human airways, *Experiments in Fluids* **56**, 1 (2015).
  - [19] E. R. Weibel, Geometric and dimensional airway models of conductive, transitory and respiratory zones of the human lung, in *Morphometry of the human lung* (Springer, 1963) pp. 136–142.
  - [20] K. Horsfield, G. Dart, D. E. Olson, G. F. Filley, and G. Cumming, Models of the human bronchial tree., *Journal of applied physiology* **31**, 207 (1971).

- [21] A. Guha, K. Pradhan, and P. K. Halder, Finding order in complexity: A study of the fluid dynamics in a three-dimensional branching network, *Physics of Fluids* **28**, 123602 (2016).
- [22] D. K. Walters and W. H. Luke, A method for three-dimensional navier–stokes simulations of large-scale regions of the human lung airway, *Journal of Fluids Engineering* **132**, 051101 (2010).
- [23] N. Nowak, P. P. Kakade, and A. V. Annapragada, Computational fluid dynamics simulation of airflow and aerosol deposition in human lungs, *Annals of biomedical engineering* **31**, 374 (2003).
- [24] C. Kleinstreuer and Z. Zhang, An adjustable triple-bifurcation unit model for air-particle flow simulations in human tracheobronchial airways, *Journal of biomechanical engineering* **131**, 021007 (2009).
- [25] K. Pradhan and A. Guha, Fluid dynamics of a bifurcation, *International journal of heat and fluid flow* **80**, 108483 (2019).
- [26] A. Menon, M. Weber, and H. Chang, Model study of flow dynamics in human central airways. part iii: Oscillatory velocity profiles, *Respiration physiology* **55**, 255 (1984).
- [27] B. Gatlin, C. Cuicchi, J. Hammersley, D. Olson, R. Reddy, and G. Burnside, Computational simulation of steady and oscillating flow in branching tubes, in *Proceedings of ASME FED Symposium on Biomedical Fluids Engineering*, Vol. 212 (1995) pp. 1–8.
- [28] S. Jalal, T. Van de Moortele, O. Amili, and F. Coletti, Steady and oscillatory flow in the human bronchial tree, *Physical Review Fluids* **5**, 063101 (2020).
- [29] S. Jalal, A. Nemes, T. Van de Moortele, S. Schmitter, and F. Coletti, Three-dimensional inspiratory flow in a double bifurcation airway model, *Experiments in Fluids* **57**, 1 (2016).
- [30] S. Jalal, T. Van de Moortele, A. Nemes, O. Amili, and F. Coletti, Three-dimensional steady and oscillatory flow in a double bifurcation airway model, *Physical Review Fluids* **3**, 103101 (2018).
- [31] M. Hino, M. Sawamoto, and S. Takasu, Experiments on transition to turbulence in an oscillatory pipe flow, *Journal of Fluid Mechanics* **75**, 193 (1976).
- [32] R. Akhavan, R. Kamm, and A. Shapiro, An investigation of transition to turbulence in bounded oscillatory stokes flows part 1. experiments, *Journal of Fluid Mechanics* **225**, 395 (1991).
- [33] R. Akhavan, R. Kamm, and A. Shapiro, An investigation of transition to turbulence in

- bounded oscillatory stokes flows part 2. numerical simulations, Journal of Fluid Mechanics **225**, 423 (1991).
- [34] D. Xu, A. Varshney, X. Ma, B. Song, M. Riedl, M. Avila, and B. Hof, Nonlinear hydrodynamic instability and turbulence in pulsatile flow, Proceedings of the National Academy of Sciences **117**, 11233 (2020).
- [35] B. B. Mandelbrot, *The fractal geometry of nature*, Vol. 173 (WH freeman New York, 1983).
- [36] J. Emery, *The anatomy of the developing lung* (Butterworth-Heinemann, 2014).
- [37] K. Koombua, R. M. Pidaparti, P. W. Longest, and K. R. Ward, Computational analysis of fluid characteristics in rigid and flexible human respiratory airway models, Engineering Applications of Computational Fluid Mechanics **2**, 185 (2008).
- [38] J. R. Womersley, Method for the calculation of velocity, rate of flow and viscous drag in arteries when the pressure gradient is known, The Journal of physiology **127**, 553 (1955).
- [39] P. F. Fischer, F. Loth, S. E. Lee, S.-W. Lee, D. S. Smith, and H. S. Bassiouny, Simulation of high-Reynolds number vascular flows, Computer methods in applied mechanics and engineering **196**, 3049 (2007).
- [40] P. F. Fischer, J. W. Lottes, and S. G. Kerkemeier, Nek5000 web page (2008).
- [41] S. E. Lee, S.-W. Lee, P. F. Fischer, H. S. Bassiouny, and F. Loth, Direct numerical simulation of transitional flow in a stenosed carotid bifurcation, Journal of biomechanics **41**, 2551 (2008).
- [42] G. K. El Khoury, P. Schlatter, A. Noorani, P. F. Fischer, G. Brethouwer, and A. V. Johansson, Direct numerical simulation of turbulent pipe flow at moderately high reynolds numbers, Flow, turbulence and combustion **91**, 475 (2013).
- [43] H. M. Tufo and P. F. Fischer, Terascale spectral element algorithms and implementations, in *SC'99: Proceedings of the 1999 ACM/IEEE Conference on Supercomputing* (IEEE, 1999) pp. 68–68.
- [44] P. C. Rimensberger, S. Schulzke, D. Tingay, and B. Von Ungern-Sternberg, Pediatric and neonatal mechanical ventilation, Geneve: Springer (2015).
- [45] W. R. Dean, Xvi. note on the motion of fluid in a curved pipe, The London, Edinburgh, and Dublin Philosophical Magazine and Journal of Science **4**, 208 (1927).
- [46] T. Pedley and R. Kamm, The effect of secondary motion on axial transport in oscillatory tube flow, Journal of Fluid Mechanics **193**, 347 (1988).
- [47] M. K. Sharp, R. Kamm, A. Shapiro, E. Kimmel, and G. Karniadakis, Dispersion in a curved

- tube during oscillatory flow, *Journal of fluid mechanics* **223**, 537 (1991).
- [48] J. R. Hill and D. Robinson, Oxygen consumption in normally grown, small-for-dates and large-for-dates new-born infants, *The Journal of physiology* **199**, 685 (1968).
- [49] J. Jeong and F. Hussain, On the identification of a vortex, *Journal of fluid mechanics* **285**, 69 (1995).